ADVANCED MATERIALS
www.advmat.de

Ultrafast Laser Processing of 2D Materials: Novel Routes to Advanced Devices

Aleksei V. Emelianov, Mika Pettersson, and Ivan I. Bobrinetskiy**

Ultrafast laser processing has emerged as a versatile technique for modifying materials and introducing novel functionalities. Over the past decade, this method has demonstrated remarkable advantages in the manipulation of 2D layered materials, including synthesis, structuring, functionalization, and local patterning. Unlike continuous-wave and long-pulsed optical methods, ultrafast lasers offer a solution for thermal heating issues. Nonlinear interactions between ultrafast laser pulses and the atomic lattice of 2D materials substantially influence their chemical and physical properties. This paper highlights the transformative role of ultrafast laser pulses in maskless green technology, enabling subtractive, and additive processes that unveil ways for advanced devices. Utilizing the synergetic effect between the energy states within the atomic layers and ultrafast laser irradiation, it is feasible to achieve unprecedented resolutions down to several nanometers. Recent advancements are discussed in functionalization, doping, atomic reconstruction, phase transformation, and 2D and 3D micro- and nanopatterning. A forward-looking perspective on a wide array of applications of 2D materials, along with device fabrication featuring novel physical and chemical properties through direct ultrafast laser writing, is also provided.

1. Introduction

Over the past two decades, ultrafast laser irradiation has demonstrated scientific, technological, and industrial potential in a wide range of applications. In particular, it has evolved into a powerful tool for maskless patterning of both 2D and 3D materials.[1] In the recent decade, laser processing has shown several advantages in applications involving 2D layered materials (2DM), such as ablation,[2] exfoliation,[3] graphene generation from other low-dimensional forms,[4] stimulated growth from the solid phase (SiC, polyimide, etc.),[5,6] laser induced chemical vapor deposition (CVD), and laser-reduced graphene oxide.[7] Despite extensive reviews on laser processing of graphene and 2DM,[8–12] there is a notable gap in the literature related to the nonlinear effects arising from the interaction of 2DM with ultrafast lasers. Ultrafast lasers offer a way to overcome the challenges of thermal heating caused by continuous-wave (CW) and long-pulsed laser irradiation. They hold promise for a green technology approach to graphene and 2D/3D materials processing through subtractive and additive techniques, with direct laser writing (DLW) enabling high speed and exceptional resolution down to several nanometers.[13–16] The interaction of ultrafast pulsed laser irradiation with the graphene lattice under various environmental conditions can result in doping,[17] functionalization,[18] reduction,[19] ablation,[20] and precise nano- and micropatterning.[21,22] It makes ultrafast laser processing a highly attractive breakthrough technology for manufacturing graphene-based devices. Furthermore, ultrafast atomic reconstruction with phase transition has been demonstrated for materials, such as carbon nanotubes,[23,24] graphene,[25] and transition metal dichalcogenides (TMDs) such as $IrTe_2$,[26] $MoTe_2$,[27] and MoS_2.[28] Compared with commonly used CW lasers[29] and UV sources,[30,31] ultrafast DLW (UDLW) offers better control over lattice modification with exceptional precision. UDLW effectively reduces heating effects, enabling the direct processing of 2D materials onto flexible substrates. Additionally, ultrafast laser spectroscopy has provided valuable insights into the charge carrier dynamics in graphene and related materials, accelerating advancements in various applications, including emerging fields, such as terahertz (THz) optoelectronics.[32]

Here, we present recent advances and a perspective outlook for ultrafast laser processing of 2DM in the application of novel optical and electronic devices. In Section 2, we discuss the fundamentals of ultrafast laser interaction with 2DM that make it valuable for desired processing methods. In Section 3, we provide a survey of the current state-of-the-art UDLW of 2D nanostructures. Finally, in Section 4, we discuss the technological perspectives of

A. V. Emelianov, M. Pettersson
Nanoscience Center
Department of Chemistry
University of Jyväskylä
Jyväskylä FI-40014, Finland
E-mail: mika.j.pettersson@jyu.fi
I. I. Bobrinetskiy
BioSense Institute – Research and Development Institute for Information Technologies in Biosystems
University of Novi Sad
Novi Sad 21000, Serbia
E-mail: bobrinet@biosense.rs

The ORCID identification number(s) for the author(s) of this article can be found under https://doi.org/10.1002/adma.202402907

DOI: 10.1002/adma.202402907

ultrafast laser processing in the advanced photonic, electronic, and sensor applications of 2DM and compare the mechanisms behind different applications of ultrafast laser modified nanomaterials.

2. Ultrafast Charge Carrier Dynamics in 2D Materials

Graphene possesses a gapless energy band structure that results in unique charge carrier dynamics. Initial investigations into the interaction of ultrafast laser pulses with 2D materials utilized ultrafast pulsed-laser spectroscopy methods. The charge dynamics of graphene and other 2DMs have been explored using techniques such as pump–probe spectroscopy,[33,34] ultrafast time-resolved photocurrent scanning microscopy,[35] ultrafast grating imaging technique,[36] femtosecond time-resolved angle resolved photoelectron spectroscopy,[37,38] and time-resolved optical pump-THz probe spectroscopy.[39,40] These time-resolved studies have identified that the energy relaxation dynamics of photoexcited carriers mainly involve carrier–carrier scattering and coupling to optical, acoustic, and remote substrate phonons.[41] Carrier–carrier scattering leads to a very rapid ($t \lesssim 50$ fs) broadening of the electron distribution as a function of energy, associated with thermalization within the electronic system, commonly referred to as carrier heating.[37,38,40,42,43]

When graphene absorbs electromagnetic radiation, its electrons heat up and produce a detectable thermoelectric response, even at room temperature.[44] Due to graphene gapless dispersion relation, small electron heat capacity, and anomalously weak electron–phonon coupling, this photothermal electron activation mechanism is broadband (from UV to visible), highly sensitive, and fast. Moreover, when exposed to high-energy photons in the 4–5 eV range, an increase in optical absorption was observed. This rise is attributed to the interband transitions of graphene from bonding to antibonding states near the distinct saddle-point singularity at the M point in the Brillouin zone.[45,46]

While relaxation dynamics have been actively studied and reliable pictures have been proposed for different graphene models,[41] excitation dynamics have been less investigated due to a very short timescale. When an ultrafast pulse, either femtosecond (fs) or picosecond (ps), excites carriers in graphene,[47] the nonequilibrium photogenerated electron and hole distributions return to equilibrium, according to the scheme shown in **Figure 1a**. The carrier generation rate upon ultrafast pulse can be evaluated using the Bloch equations in the weak pump limit[48]

$$\frac{\partial f}{\partial t} = \sqrt{\frac{\pi}{2}}\frac{e^2 v_F^2 w}{2\hbar^2} A_o^2 \left|\sigma_{cv}^{\lambda}\right|^2 e^{-\frac{t^2}{2w^2}} e^{-\frac{w^2\delta^2}{2}} \left(f_v - f_c\right) \times \text{Real}\left[e^{-i\delta t}\left(1 + \text{Erf}\left(\frac{t}{\sqrt{2}w} - \frac{i\delta w}{\sqrt{2}}\right)\right)\right] \quad (1)$$

where v_F is the Fermi velocity in graphene, w is the pump pulse width, t is time, and f_v and f_c are the distribution functions of charge carriers in valance and conduction bands, respectively. Erf is the error function, A_0 is the vector potential amplitude of the pulse, and δ is the detuning (difference between the pulse central frequency and medium transition frequency). The factor $|\sigma_{cv}^{\lambda}|^2$ implies the interband matrix element of the sublattice Pauli matrix in the (kx; ky) plane for a linearly polarized pump pulse with polarization in the λ direction.

The charge carriers are generated anisotropically by the polarized pump pulse, according to the matrix element $|\sigma_{cv}^{\lambda}|^2$ in Equation (1). Thermalization occurs, and subsequently the hot carriers are cooled by interacting with the lattice.[48] In photovoltaics, these carriers accelerate in the presence of an electric field, resulting in time-dependent photocurrent.

The distribution of charge carriers on the energy scale $N(E)$ can be evaluated. $N(E)dE$ is the carrier density between the energies E and $E + dE$, which gives the total carrier density by integration over all energies. This energy distribution was evaluated using Equation (2)

$$N\ (E) = \iint \frac{dk}{(2\pi)^2} f\ (k)\ \delta\left(\varepsilon_k - E\right) \quad (2)$$

Figure 1b illustrates the carrier generation by optical pulses in pristine graphene. The carrier dynamics during the excitation was nontrivial. As long as the charge carrier lifetime in graphene is about 1 ps,[49] the defined diffusion length (without an applied electric field) is almost constant for various carrier densities and is ≈1.4 µm.[36] This results in an unprecedented diffusion coefficient D ≈10 000 cm^2 s^{-1} and mobility µ ≈120 000 cm^2 V^{-1} s^{-1} due to the high photoexcited carrier energies.

Key relaxation mechanisms include "Thermalization" and "Cooling" (Figure 1a). Initial and photoexcited carriers thermalize to a drifted "Thermalized Fermi–Dirac" equilibrium distribution within tens of femtoseconds[51] and to an effective carrier temperature T_e, which is higher than the lattice temperature T due to the pumped energy in the system.[48,52,53] This eventually cools the system to a "Cooled Fermi–Dirac" distribution over hundreds of femtoseconds, aligning with lattice temperature T. Hot thermally distributed carriers cool due to intraband phonon scattering. Interband recombination occurs over a much longer timescale than thermalization and cooling.

Hot electron relaxation typically occurs within hundreds of femtoseconds, while the lifetime of optical phonons is about 2.5 ps.[43] The difference between interband and intraband scattering is schematically shown in Figure 1c. Decrease in interband scattering (also called impact ionization or carrier multiplication) due to the states filling of unthermalized electrons is mainly related to the first stage of carrier photoexcitation, while a rise in intraband scattering due to free carrier absorption is responsible for hot carriers generation, also known as impact excitation or Auger heating.[34,36,41]

Impact ionization plays a dominant role in carrier generation, while intraband scattering, Auger recombination, and electron–phonon scattering do not generate new charge carriers in graphene. For single-layer graphene, the relaxation time estimates are ≈8 fs for carrier–carrier scattering, 50–120 fs for carrier thermalization, 0.1–1 ps for carrier cooling, and 3–15 ps for carrier recombination.[49]

Two primary cooling mechanisms were identified for the ultrafast pulsed laser photoexcitation of a nonideal graphene lattice.[54] (I) Supercollision cooling,[55] which produces nonmomentum-conserving transitions during disorder-assisted scattering, occurs near the charge neutrality point (Figure 1d).[44,56] (II)

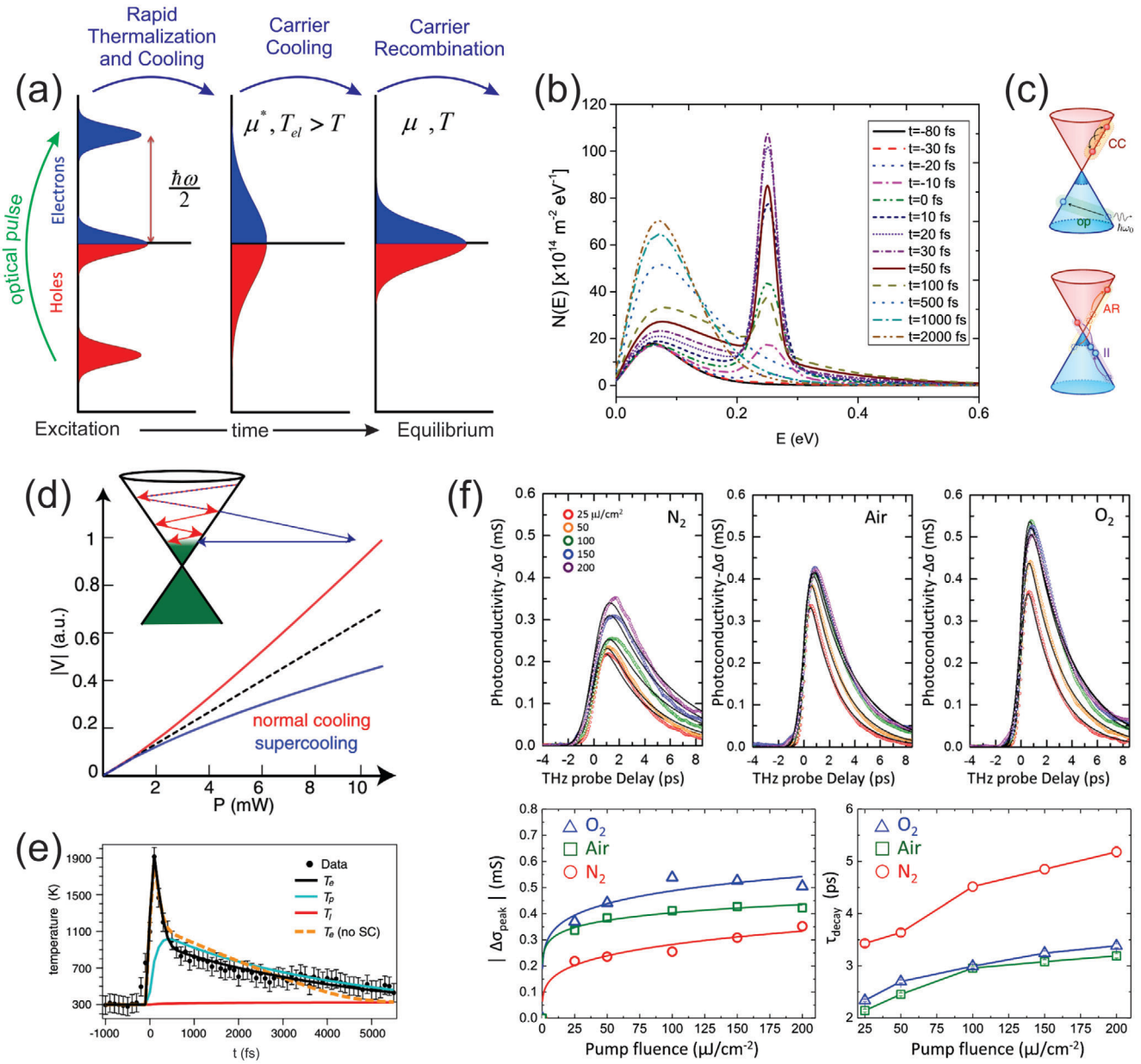

Figure 1. Ultrafast charge carrier dynamics in photoexcited graphene. a) Charge carrier photoexcitation and relaxation mechanisms include "Thermalization" and "Cooling" terms. Adapted with permission.[47] Copyright 2008, American Chemical Society. Adapted with permission.[48] Copyright 2016, American Physical Society. b) Time evolution of charge carrier distribution for undoped graphene as a function of energy for 40 fs laser pulse. Reproduced with permission.[48] Copyright 2016, American Physical Society. c) Schematic illustration of carrier scattering processes in graphene: carrier–carrier scattering (CC), optical phonon scattering (op), impact ionization (II), and Auger recombination (AR). Reproduced with permission.[49] Copyright 2012, American Physical Society. d) Calculated photothermoelectric voltage (in arbitrary units) versus input optical power for supercollision (blue) and conventional (red) cooling, illustrating sublinear and superlinear behavior, respectively. Inset: energy diagram, illustrating two different cooling mechanisms. Reproduced with permission.[44] Copyright 2016, American Physical Society. e) Electron temperature T_e in monolayer graphene as a function of time delay after fs-laser pulse. The data fit to the three temperature model provided an electronic temperature fit with (solid black line) and without (dashed amber line) the supercollision (SC) term. From the fit, the temperatures of the optical phonons (solid blue line) and the acoustic phonons (solid red line) were also obtained. Reproduced with permission.[38] Copyright 2013, American Physical Society. f) Transient photoexcited THz negative conductivity in graphene for different laser pump fluences in N_2, air, and O_2. Peak values of the photoexcited negative THz conductivity and carrier relaxation time extracted from fits as a function of a pump fluence. Adapted with permission.[50] Copyright 2017, AIP Publishing.

Conventional momentum-conserving electron–phonon cooling takes place at high charge carrier concentrations.[44,57] Finally, the recombination process between electrons and holes continues until the equilibrium distribution is restored.

The evolution of the electron temperature (T_e) in graphene is described by nonlinear differential Equation (3)

$$I\ (t) = \alpha T_e \frac{dT_e}{dt} + \beta_1 \left(T_e - T\right) + \beta_3 \left(T_e^3 - T^3\right) \quad (3)$$

where T is the lattice temperature, αT_e is the specific heat of the graphene carriers, β_1 and β_3 are the rate coefficients for the conventional and supercollision cooling mechanisms, respectively, and $I(t)$ is the absorbed optical intensity.

Ultrafast optical pulses can significantly disturb the electron temperature and, in some cases, excite high energy optical phonons[58] (hot phonons) in addition to acoustic phonons.[40,43,59] This can increase the carrier scattering rate.[41,60] Despite the electron-optical phonon scattering time is in the range of tens of femtoseconds to picoseconds,[33,37] electron diffusion has minimal impact on T within such a short timescale. This optical phonon-mediated cooling reduces the carrier T from ≈3000–3500 K[43,49,51] to ≈400 K.[35,57,61] A temporal diagram of the temperature evolution of hot electrons in graphene after fs-laser illumination is shown in Figure 1e.[38] Subsequent cooling of the electrons occurs through gradual coupling to acoustic phonons, which takes place over timescales of ≈100 ps to 10 ns, depending on the charge carrier density.[61]

In practical applications of UDLW in 2DM, the environment must be considered. Ultrafast energy relaxation processes depend on the Fermi energy of 2DM, which can be altered in different gas mixtures, and the density of excited carriers, which can change by photoexcitation fluence.[50] The adsorption of molecules on 2DM can introduce or reduce the number of physically adsorbed dopants, shifting the Fermi energy level in these regions and thus affecting the density of intrinsic carriers. When the graphene surface adsorbed gas molecules, the density of the photoexcited carriers changed and the relaxation time of the doped graphene increased (Figure 1f). Therefore, the presence of molecules near or at the surface should increase the density of intrinsic charge carriers and the heating efficiency upon photoexcitation. Moreover, the rise in electron temperature induced by photon absorption leads to a reduction in the chemical potential, maintaining a constant total carrier count in the conduction band. As the energy of the Fermi level decreases, the heating efficiency diminishes due to the slower intraband carrier–carrier scattering processes.[62]

Recently, charge carrier dynamics have been studied in novel semiconducting 2DM, such as phosphorene[63] and mono- and dichalcogenides SnS and TiS_2,[64,65] revealing a mechanism similar to graphene, as shown in Figure 1c. The electrons were excited to high energies in the conduction band during the first 400 fs through the Franck–Condon transition, leaving holes in the valence band. The cooling dynamics of semiconducting nanosheets can be divided into two processes. Initially, the electrons undergo thermal equilibrium in the conduction band within 873 fs, and then the hot electrons cool down to the valence band and recombine with the holes within a lifetime of 97 ps. Thus, the timescales for these materials are approximately ten times longer than for pristine graphene due to the presence of a bandgap.

The electron dynamics in MoS_2 under ultrafast laser irradiation have been investigated through experiments and simulations.[66] The monolayer exhibited an intraband relaxation rate more than 40 times higher than that observed for thick crystals. This enhancement was attributed to defect-assisted scattering. Monolayer and few-layer structures showed faster electron-hole recombination due to quantum confinement effects, resulting in an indirect-to-direct bandgap crossover. In thin MoS_2 flakes, nonradiative relaxation pathways dominate over radiative ones.[67] The carrier recombination time at low temperatures was about several ps,[68] and insignificant polarization decay was observed over the entire emission duration.[69] At room temperature, a direct quasiparticle bandgap of 1.95 eV was determined, along with an ultrafast (50 fs) extraction of excited free carriers via metal contacts with MoS_2,[70] which is of key importance for optoelectronic applications that rely on separated free carriers rather than excitons. In thicker MoS_2 flakes, the strain affects the electronic relaxation time.[71] Wrinkling enables larger amplitude movements of MoS_2 layers, relaxes selection rules for electron–phonon coupling, disrupts chemical bonding, and enhances the electronic density of states, leading to faster relaxation dynamics compared with flat MoS_2 flakes. Hence, applications demanding long-lived hot carriers, such as hot electron-driven light harvesting and photocatalysis, should utilize wrinkle-free TMDs.

3. Photochemical and Photophysical Effects in Ultrafast Laser Processing of 2D Materials

The previous section described the differences in the fundamental interactions between ultrafast laser light and matter at various timescales. Based on this knowledge, here we focus on the UDLW of 2DM by tuning their properties via thermal and/or chemical processes. The energy range and pulse duration play a significant role in ultrafast laser processing.[72] In principle, using fs pulses one can control the type of light–matter interaction, while in real experiments the doping level and environment highly affect the carrier dynamics.[50] Nevertheless, DLW is a useful tool to pattern and activate the surface locally and on a large scale, attach various species, induce phase transition and selective growth, and modify thermoelastic, optical, and electronic properties. Ultrafast laser irradiation allows for the patterning of 2DM on diverse substrates without inducing significant heating effects, finding applications in biology, medicine, etc. Moreover, UDLW can be used to create 3D structures from 2DMs.

3.1. Reduction of Graphene Oxide

Graphene oxide (GO) attracts huge attention as an industrially scalable material due to its relatively simple production techniques, compatible with cost-effective printing methods, such as screen-printing,[73] inkjet printing,[74] spray coating,[75] roll-to-roll process.[76] This makes maskless processing methods highly desirable for tuning the properties of GO for various applications. The presence of oxygen-containing groups (carboxyl, epoxy, hydroxyl, carbonyl, etc.), other sp^3 defects, and vacancies makes GO

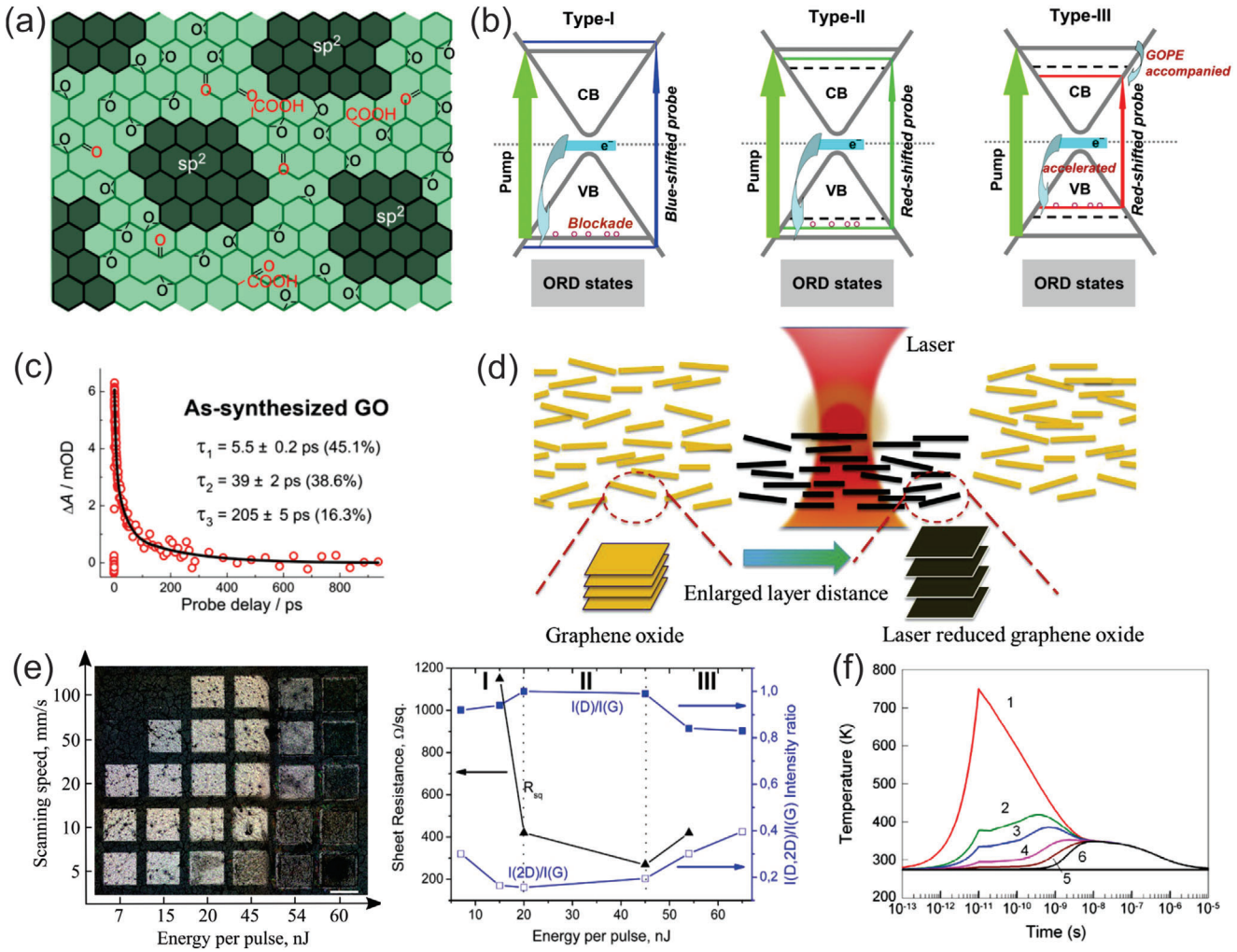

Figure 2. Interaction of ultrafast laser pulses with graphene oxide. a) Schematic model of GO structure consisting of randomly distributed graphene-like domains and large-area oxygen-rich domain (ORD). Adapted with permission.[81] Copyright 2012, American Chemical Society. b) Three types of kinetics observed in as-synthesized GO probed by pulsed lasers with different wavelengths: type I – hole blockade effect for blue-shifted probe pulse, types II and III — G-mode optical phonon emission (GOPE) for redshifted probe pulse with photon energy higher and lower than GOPE, respectively. Localized impurity states are shown in the bandgap. Adapted with permission.[82] Copyright 2013, American Chemical Society. c) Typical charge carrier kinetics of GO film after ultrafast laser pulse. Reproduced with permission.[82] Copyright 2013, American Chemical Society. d) Schematic illustration of the laser reduction of GO film revealing the photochemical and geometrical patterning. Reproduced with permission.[84] Copyright 2019, Elsevier. e) GO film exposed to fs-laser pulses with varying energy and scanning speed and three typical stages of GO reducing correlated with sheet resistance and Raman signal evolution (for 20 mm s^{-1} scanning speed): I – chemical reduction, III – thermal reduction, II – both stages. Adapted with permission.[85] Copyright 2017, Elsevier. f) Heat transfer in GO film after a single 10 ps 1064 nm laser pulse of 0.2 μJ (20 mW) at different depths. From 1 to 6: GO surface, 300, 500, 700, and 900 nm under the surface, and at the GO and PC substrate boundary (1200 nm), respectively. Reproduced with permission.[19] Copyright 2013, Elsevier.

a low conductive material and demands for its reduction to attain conductivity close to graphene.[77] The technology for large-scale production and deposition of graphene from graphene oxide ink is well-developed.[78] GO thick films also find their use in the formation of 3D structures for microfluidics and wiring interconnections.[79,80]

The structure of GO continues to be a topic of research and discussion. The prevailing model suggests two domains within GO: a carbon-rich, graphene-like domain characterized by oxidatively hybridized graphene sheets with significantly larger dimensions than the randomly distributed nanometer-sized sp^2 clusters, and a large oxygen-rich domain (**Figure 2a**).[81] This model gains support from both ultrafast (≈100 fs) and "ultraslow" (≈200 ps) processes observed in highly oxidized GO through pump–probe experiments.[82]

The ultrafast cooling mechanism (Figure 2b) of photoexcited electrons via carrier-optical phonon scattering (within a few hundreds of fs) and carrier-acoustic phonon scattering (within a few ps) is similar to that in pristine graphene.[40,43,58,59] In contrast, the slower components of this relaxation process, characterized by relaxation times ranging from a few tens to a few hundreds of ps, are attributed to the release of trapped electrons from different trap depths within the oxygen-rich domain (Figure 2c).[83] Figure 2b also demonstrates that by tuning the

wavelength of the fs pulse, each of these relaxation paths can be addressed.

Different methods have been implemented to produce reduced GO (rGO), including chemical,[86] thermal,[87] electrochemical,[88] and light-assisted treatment.[89] Among these, the light-assisted method, specifically DLW, is the most attractive because it provides a precise impurity-free control ratio of carbon and oxygen atoms with sp^2 bonds restoration,[7] maskless patterning with submicrometer resolution and high-speed,[90] facilitating easy integration with other GO printing methods (Figure 2d). Scanning speeds up to 0.1 m s^{-1} have been achieved while maintaining reproducible rGO characteristics (Figure 2e).[85]

The reduction mechanism of GO through UDLW involves several factors affected by laser irradiation. The spatial energy delivered to the material controls the temperature profile during processing. To analyze the reduction mechanism via UDLW, we need to consider various aspects, including thermalization, photoionization, and electron solvation in water.[91] Notably, electron solvation in water was suggested as a predominant factor in the water-assisted reduction of GO under UV UDLW. Understanding the precise dynamics of charge carriers in GO during fs pulsed UV laser oxidation in the presence of water molecules reveals the complexity of the reduction processes. Only mobilized solvated electrons could induce a reduction within a relaxation time of 250 ps. Thus, radiation chemistry plays a major role in the ultrafast reduction of GO. Moreover, multiphoton processes can significantly impact the interaction between the materials and their environment.[85]

The duration, energy, and repetition rate of a laser pulse determine the photoreduction process. The photoreduction mechanism of GO by the fs-laser at a lower power is similar to the photochemical reduction of GO under continuous UV irradiation[81] and electrochemical reduction,[92] where both the transformation of water to oxygen and carbon dioxide generation play a significant role.[93] Photothermal effects dominate in the restoration of sp^2 bonds, while photochemical processes are responsible for the removal of oxygen functional groups (Figure 2e).[19,84,85,94] Photothermal processes occur at any wavelength of a pulsed or CW laser associated with photon absorption, leading to hot-electron generation and further relaxation via acoustic phonons, resulting in lattice heating. In simulations involving the linear absorption of GO films, a temperature rise exceeding 700 °C was observed following a 10 ps pulse with an energy of 0.2 μJ,[19] and it lasted for ≈10 ns, which is typically less than the time interval between two ultrafast pulses (0.1–10 μs) (Figure 2f). Therefore, the cooling time of the GO sheet was shorter than the interval between the laser pulses, and the accumulation of heat between the laser pulses could be neglected. The increased temperature also affected the oxidative groups detachment and healing of the honeycomb lattice.

When photochemical effects prevail during the reduction process, it involves the direct breaking of chemical bonds between carbon and oxygen atoms, such as C—O or C═O bonds, leading to the removal of oxygen species,[84,95] especially when the photon energy exceeds 3.2 eV (UV light).[96] At lower photon energies, nonlinear effects such as multiphoton absorption can initiate the photoreduction of GO.[85,97]

The use of ultrafast laser pulses provides flexibility in tuning the electrical, optical, and structural properties of rGO. For example, degradation of carbonyl groups was observed in rGO patterned via a UV fs-laser.[82] For visible range ps-laser irradiation, the reduction process of monolayer GO flakes on a substrate led to a decrease in hydroxyl groups.[98] Ab initio calculations demonstrated that the carbonyl groups in GO primarily contribute to impurity states within the graphene matrix, while epoxy or hydroxyl groups play a role in bandgap tuning and doping.[82] By altering the ultrafast laser wavelength, it is possible to selectively detach specific oxygen species,[84,98] by considering their binding energies with graphene.[99,100]

3.2. Two-Photon Oxidation

The recently developed laser-induced two-photon oxidation (TPO) method has enabled precise control of the oxidation conditions in single- and few-layered graphene, offering potential applications in graphene-based electronic and optoelectronic devices using an all-optical approach.[101–104] This method relies on two-photon processes in ultrafast laser oxidation, which have been studied by nonlinear spectroscopy and imaging[105] and experiments at various wavelengths,[101,103,106] indicating the interactions between light, carbon lattice, oxygen, and water molecules. This method was initially developed during the oxidation of single-walled carbon nanotubes[107] and was later applied to fabricate highly sensitive visible-light detectors.[108]

During UDLW, multiple processes occur involving graphene, the substrate, and the surrounding environment. Although graphene absorbs only 2.3% of visible light,[109] the actual optical absorption may be higher due to light interference with the substrate.[2] The thermalization process in graphene occurs within a timescale similar to the fs-laser pulse duration, but relaxation via phonons takes much longer, around several ps. Hence, there is almost no heating of the graphene surface during the fs-laser pulse duration.[53]

Two-photon absorption (TPA) is a key mechanism in the photochemical oxidation of graphene, which involves the formation of charged oxygen species.[110] This process can be enhanced by the generation of water radicals and solvated electrons via TPA, especially at higher humidity levels.[91,111]

The growth mechanism of TPO graphene upon fs-laser pulses was studied at a high resolution down to 300 nm, revealing that it initiates from seed points and extends to GO islands, as shown in **Figure 3a**.[112] This model supports the two-domain model of GO production,[82,113,114] resulting in two distinct regions characterized by different energy structures fine-tuned by the fs-laser. The narrow graphene channels between the oxide islands resemble nanoribbons, with their width dictating the bandgap energy, which increases as the graphene areas become smaller. Therefore, the merging of these islands disrupted the conductive graphene channels. At this point, the electrical properties are determined by GO, which behaves as a semiconductor or insulator depending on the level of oxidation. The chemical composition of TPO graphene mostly consists of hydroxyl and epoxy groups (Figure 3b)[115] that make this kind of graphene oxide structurally more ordered compared with the chemically produced GO.[98] Moreover, the saturated atomic concentration of hydroxyl groups

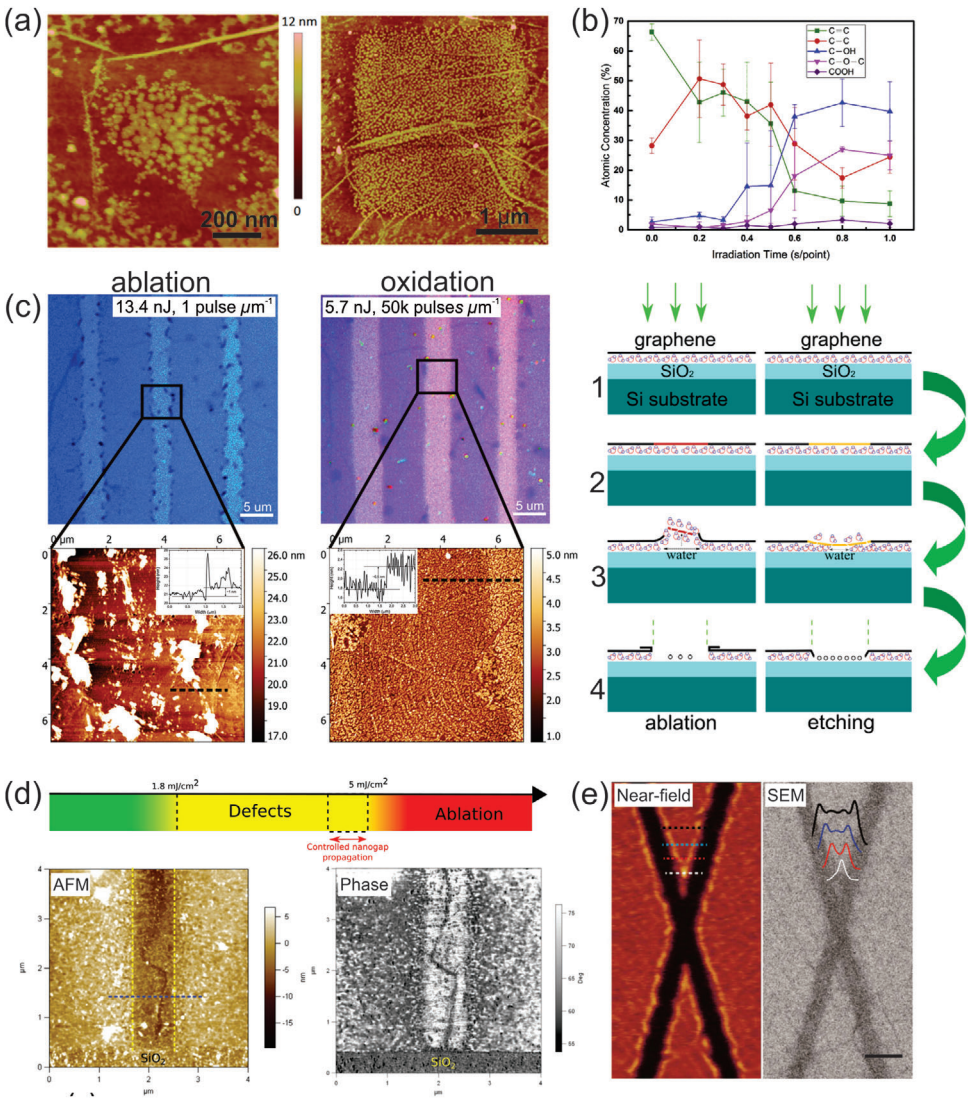

Figure 3. Two-photon oxidation of graphene upon fs-laser irradiation. a) TPO on pristine graphene surface in a single spot within 2 s with a tightly focused laser beam and square array made by oxidizing a matrix of spots with 100 nm spacing. Adapted with permission.[112] Copyright 2016, American Chemical Society. b) Chemical composition of photo-oxidized graphene at different time of laser irradiation. Reproduced with permission.[115] Copyright 2017, Elsevier. c) Comparison of ultrafast laser ablation and oxidation of graphene. Ablated lines in graphene after 280 fs laser processing with 13.4 nJ, 1 pulse per μm and oxidized at 5.4 nJ, 50 000 pulses per μm. Schematic diagram presents the ultrafast laser-induced ablation and oxidative etching processes. Reproduced with permission.[116] Copyright 2016, IOP Publishing. d) A graphene nanogap-based device after laser pre-patterning and electroburning, and a diagram representing the effect of increasing laser fluence on graphene. The defect line is highlighted between the two yellow dashed lines. The nanogap corresponds to the dark zigzagged line in the middle of the image. Reproduced with permission.[117] Copyright 2018, John Wiley and Sons. e) Near-field distributions of a laser patterned "X" structure at an excitation wavelength of 9.588 µm and corresponding SEM image. Scale bar is 500 nm. Adapted with permission.[118] Copyright 2018, Optica Publishing Group.

of TPO graphene was around 40%, while the concentration of epoxy groups reached only 25%. The calculations predicted an energy gap of 2 eV and a Fermi level near the valence band for graphene functionalized with epoxy groups at a C/O ratio of 2/1, however, no bandgap was observed for graphene with the same concentration of carbonyl groups.[82]

The TPO process is initiated by the formation of point-like functionalized sites, characterized as local sp^3 defects or vacancies.[119] These point defects were generated by UDLW during the initial phase of the electron thermalization process.[120] Experiments conducted with graphite in a high vacuum environment have shown that these defects coalesce to form 5 nm strained domains, and their number depends on the applied laser pulses.[121] In the presence of oxygen and water, these initial point defects grew into nanosized islands due to further surface oxidation. This transformation is remarkably more favorable (approximately five orders of magnitude) compared to the oxidation of pristine areas.[115]

Recently, TPO was also observed in MoS_2 films.[122] The process starts with the generation of sulfur vacancies via UDLW and further adsorption of oxygen molecules from air. It was demonstrated via density functional theory (DFT) that oxygen molecules

chemisorbed at vacancies form a substitutional oxygen atom and one oxygen atom bonded to a sulfur atom that was strongly bound to the MoS_2 lattice. Interestingly, the bandgap of TPO MoS_2 is very close to a pristine flake but differs significantly from MoS_2 with S vacancies.

The ablation or etching threshold of graphene and other 2DM is easily achieved by increasing the laser fluence.[15,116] Using UDLW, it is possible to realize these two processes independently. Ablation, predominantly photothermal or photoelastic in nature, initiates the melting of the carbon lattice[20] or the repulsive detachment of graphene through an acoustic shockwave[123,124] and their combination, resulting in rather nonuniform ablated graphene edges (Figure 3c).[116] Etching, or complete oxidation, occurs as a consequence of multiple oxidation processes, requiring many pulses with energies below the ablation threshold.[103,116] A longer irradiation time at lower pulse energies led to the accumulation of defects and subsequent graphene etching. The TPO model is also valid for CW lasers, but due to the lower probability of TPA processes, oxidation may require minutes[125] or even hours.[110] In contrast, by utilizing ultrafast laser pulses, this process can be achieved within a single pulse[102] that makes graphene processing unprecedently fast. Thus, UDLW opens the door for ultrafast photochemical patterning of other 2DM previously processed by CW lasers.[126,127]

During UDLW, the generation of hot carriers promotes the photoinduced desorption of oxygen.[128,129] The associated energy relaxation time scale was found to be extremely fast, ≈100 fs. This rapid energy dissipation, driven by hot electrons, suggests that a nonthermal mechanism governs the desorption pathway. However, this rapid dissipation of energy by hot electrons may reduce the efficiency of the photochemical processes in graphene.[18]

The initial oxygen-binding sites on graphene are still under debate. DFT calculations of the binding energies[130] along with the stability of oxygen absorption on graphene at room temperature[131] propose that the binding sites are primarily located at defect sites, with the surface interaction playing a secondary role. The process of ultrafast laser-induced desorption of oxygen molecules in vacuum is reversible when graphene is exposed back to vacuum. However, even at a low laser fluence, CW laser processing causes photoinduced defect formation in the carbon lattice[129] and increases the binding energy to oxygen.

Maurice et al. applied UDLW to initiate the formation of nanogap in graphene via electroburning, which is a promising tool for fabricating molecular electronic devices.[117] When the lateral sizes of the defect-free graphene regions reached 2–7 nm after fs-laser processing, the authors used a low bias voltage to guide defect formation in the layer (Figure 3d). UDLW helped to localize the defective areas and limit the extent of nanogap formation.

Ultrafast laser pulses can interact with materials other than oxygen and water to trigger the TPO of graphene. Xu et al. have shown that the multiphoton oxidation of graphene via redox reactions with silica is suitable for plasmonic waveguide formation, demonstrating a resolution down to 100 nm (Figure 3e).[118] Moreover, the resolution of fs-laser patterning on graphene and other 2DM can be reduced to ≈10 nm when employing orthogonally polarized double fs-laser beams, as has been demonstrated for silicon surfaces.[16]

3.3. Optical Forging

Manipulation of local mechanical properties by ultrafast laser pulses is one of the latest intriguing discoveries in the field of light–matter interaction. At a high excitation power, the hot charge carriers and optical phonon modes reach quasiequilibrium. The decay of the electron temperature during this stage is governed by the relaxation of optical phonons.[58,59,62] After intense irradiation, the photoexcited carriers undergo rapid thermalization and dissipate energy to the optical phonons. Most electrons have energies below the threshold for optical phonon emission (≈0.2 eV).[43,132] This leads to a cooling bottleneck effect, determined by factors such as the supercollision-cooling kinetic rate and intrinsic disorder.[56] These effects result in the mechanical expansion and contraction of graphene within the timeframe of the acoustic phonon relaxation.[61]

Hu et al. used ultrafast electron crystallography to investigate how excitations and the anharmonic interactions of various phonon modes modulate the rippling structure of suspended monolayer graphene after fs-laser irradiation (**Figure 4a**).[133] After 5 ps of the pulse, the pressure within the graphene layer rapidly increased, causing expansion due to the excitation of nonthermal in-plane longitudinal (LA) and transverse acoustic phonons (TA). This dynamic behavior is consistent with the lifetimes of optical and acoustic phonons and may be attributed to a rapid transition from optical phonons to in-plane acoustic phonons. Although rapid lattice expansion was observed within the first 5 ps, the subsequent recovery and formation of ripple structures over the next 50 ps led to layer contraction. This process involves an increase in out-of-plane thermal fluctuations and a rise in the population of out-of-plane phonon modes (ZA). This expansion/contraction mechanism aligns well with the experimental observations of strain dynamics. The layer contraction and ripple formation were enhanced with increasing laser fluence. The effect of expansion/contraction within the same timescale has been previously observed in graphite samples.[134] However, the key factor in engineering strain within graphene layers is the generation of strongly coupled optical phonons induced by ultrafast laser illumination, resulting in the expansion of graphene layers along the *z*-axis. Reversible and nonreversible tensile elastic strain of graphene and formation of local 3D structures can be utilized in many applications in plasmonics and straintronics.[135]

Unique manipulation of the elastic properties of graphene by UDLW was recently demonstrated for single-layer graphene supported on a substrate in an inert atmosphere.[136,137] UDLW led to the formation of 3D structures from the 2D graphene layer, including blisters and ripples, with controllable height and geometry at subwavelength resolution (Figure 4b). The formation of blisters can be explained by the local expansion of the graphene membrane due to laser-induced defects and the resulting compressive in-plane stress. The spatial profile of the laser intensity plays a crucial role in determining the local expansion field, allowing precise control over the expansion, blister height, and number of ripples by varying the irradiation time (Figure 4c). Characterization of the mechanical properties of graphene via AFM revealed reduced adhesion in the irradiated areas compared with pristine graphene, indicating detachment from the substrate.[139] When writing elements overlapped, extended

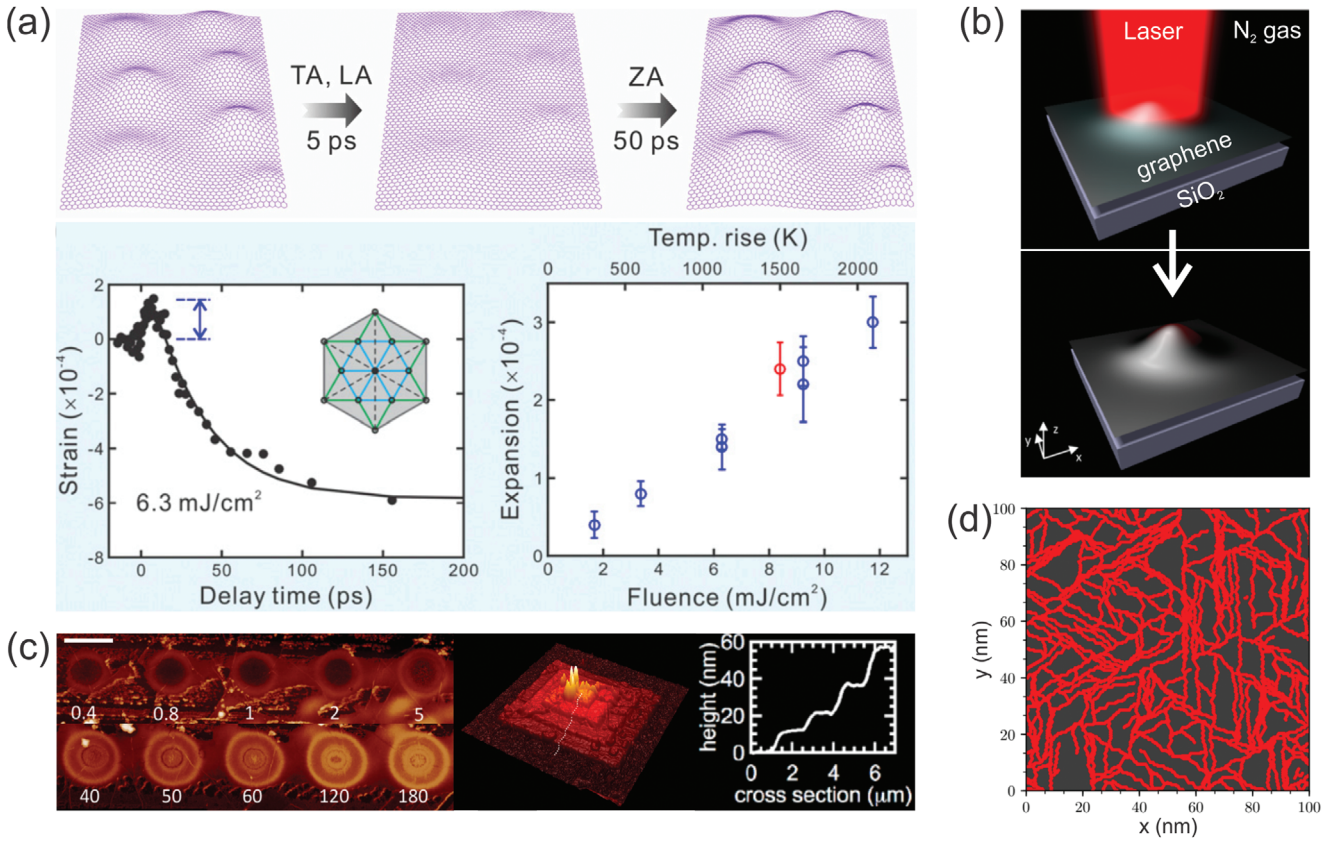

Figure 4. Mechanical modification of graphene by femtosecond laser pulses. a) Temporal evolution of the in-plane strain derived by monitoring the change of the Brillouin zone area. Reproduced with permission.[133] Copyright 2016, National Academy of Sciences. b) Scheme of the gradual formation of optically forged graphene blisters on SiO_2. Adapted under the terms of the CC-BY license.[136] Copyright 2018, American Chemical Society. c) AFM images of optically forged single blisters formed at progressively increasing irradiation time (shown in seconds) and stepwise increasing of irradiation levels (right). Scale bar is 1 μm. Adapted under the terms of the CC-BY license.[136] Copyright 2018, American Chemical Society. Adapted with permission.[137] Copyright 2017, American Chemical Society. d) Model of Stone–Wales line defect-defined crystallites growth. Reproduced with permission.[138] Copyright 2020, American Chemical Society.

patterns were formed, and their shapes followed a simple geometric rule. Optical forging can be used to substantially enhance the bending stiffness of monolayer graphene by forming fully stable corrugated structures.[140]

This model of defect generation by UDLW demonstrates similarities with the mechanisms previously discussed for TPO in an oxygen-containing atmosphere. By changing the environmental conditions, graphene can be selectively oxidized without forming ripples or ripples can be induced without oxidation,[136] providing an additional layer of control over the graphene properties. Additional degrees of freedom can be achieved by tuning the competitive relaxation mechanisms of hot electrons in graphene between carrier–carrier scattering and optical phonon emission.[62] UDLW can initiate the formation of Stone–Wales defects from point defects,[141] introducing local disorder and facilitating graphene reconstruction in a vacuum or an inert atmosphere (Figure 4d).[138] Moreover, the sizes of single ripples can reach 100 nm, which is ≈10 times smaller than the beam diameter. Therefore, the optical forging and formation of graphene 3D structures go far beyond the diffraction limit. The localized confinement of Dirac fermions in laser-induced strained graphene holds the potential for advanced electronic applications, including memory and quantum computing.[142]

The adhesion between graphene and the substrate is lower than for clean interfaces of van der Waals (vdW) heterostructures,[136] and various surface parameters such as the presence of water and functional groups, substrate topography, and the number of charge trap sites can affect the graphene rippling process.[143] This process can also be applied to strain engineering in other 2DM, either through thermoelastic modification or local oxidation, as recently demonstrated for TMDs using CW and fs-laser irradiation.[122,144,145]

3.4. Thinning

Thinning of graphene using lasers involves two primary effects: thermal and nonthermal. CW laser thinning of graphene and other 2DM, in general, is driven by heat transfer through the absorption of photons and subsequent energy dissipation via phonons (thermal effect).[146,147] Ultrafast laser thinning occurs differently. The energy from the fs-laser pulse is transferred at much higher rates than the phonon relaxation time, leading to

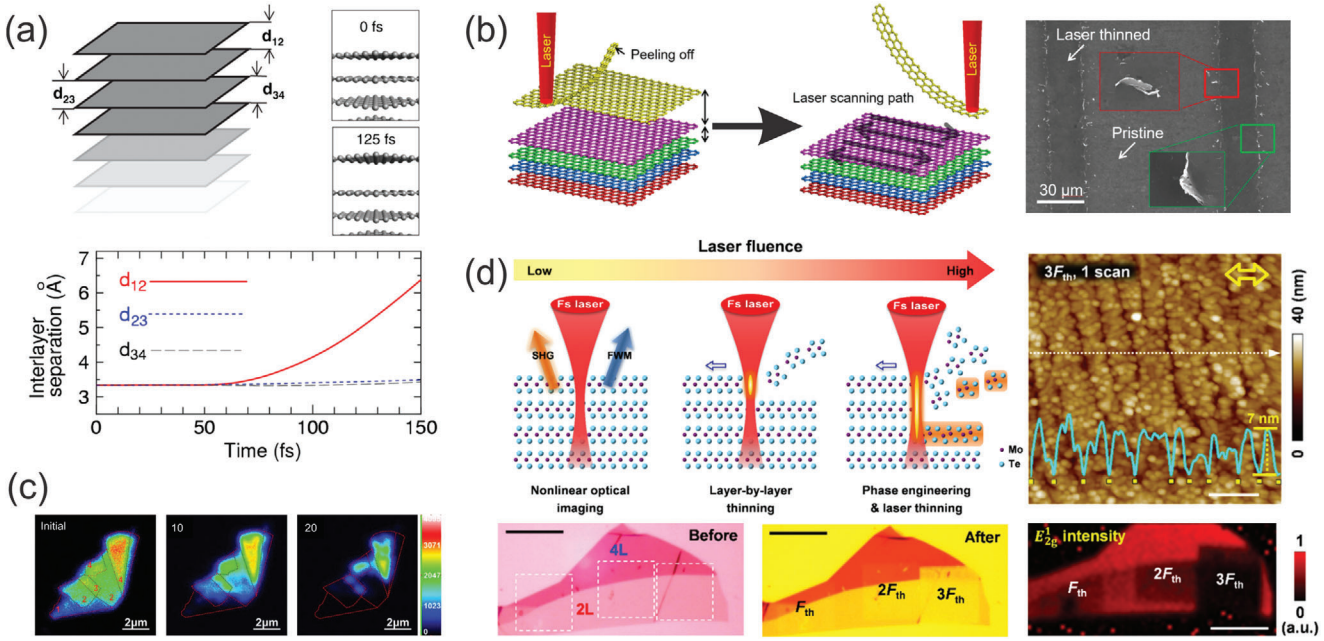

Figure 5. Ultrafast laser thinning of graphene. a) Structural change in interlayer distances of graphene stack during exposure upon 45 fs laser pulse. Reproduced with permission.[149] Copyright 2010, American Physical Society. b) Picosecond laser thinning and non-uniform edges in graphene after peeling off the material. Adapted under the terms of the CC-BY license.[150] Copyright 2015, Springer Nature. c) FWM images of layer-by-layer thinning of graphene with different number of layers and increasing fs-laser illumination time, adopted from. Adapted with permission.[148] Copyright 2015, Royal Society of Chemistry. d) Schematic view of different interactions between $MoTe_2$ layers and fs laser by varying the laser fluence. AFM topography image of the irradiated $MoTe_2$ with a laser fluence of $3F_{th}$ for one scan (the scale bar is 200 nm). Optical images and E^1_{2g} intensity map of a few-layer $MoTe_2$ consisting of a 4L region and a 2L region before and after irradiation by a fs-laser with fluences of F_{th}, $2F_{th}$, and $3F_{th}$ (the scale bar is 10 μm). Adapted with permission.[27] Copyright 2020, American Chemical Society.

the rapid cooling of hot electrons through phonon interactions, minimizing the thermal effect.[54] Therefore, nonthermal effects play an important role in the layer-by-layer thinning of 2DM.[148]

A mechanism involving Coulomb repulsion detachment was proposed to explain the exfoliation of graphene induced by fs-laser illumination.[149] In this scenario, hot electrons are removed from the surface within a fs-laser pulse (typically 10–150 fs) before thermalization begins. The exposure of the graphite surface resulted in the detachment of the topmost layer with a kinetic energy exceeding 1 eV $atom^{-1}$. Electronic excitation modifies the force field between the graphene layers, reducing the interlayer interactions. Coulomb interactions among charged graphene monolayers then drive the removal of strongly hole-doped top and bottom layers, while weakly hole-doped subsurface layers are retained due to interactions with bottom electron-doped layers (**Figure 5a**). This effect was also observed for ps-laser pulses (Figure 5b).[150] By adjusting the laser energy, it was possible to simultaneously detach a certain number of layers from the graphite surface. However, the ps-laser-induced detachment mechanism involves bond breakage at the grain edges and repulsive detachment of the material with nonuniform edges. Fs-laser illumination was also utilized to change the interlayer distance in multilayer GaSe, visualized by optical second-harmonic generation.[151] The distance could be fine-tuned via laser fluence, however, the increased interlayer distance in multilayer GaSe was not reversible.

In a humid atmosphere, both laser-induced exfoliation and photochemical oxidation are possible.[101,116] The ultrafast oxidative laser thinning of graphene is nonthermal and allows for precise thinning to a single atomic layer by selecting the appropriate fs-laser fluence and scanning times (Figure 5c). As shown for TPO of graphene, it is more favorable to oxidize a single region rather than generate new oxide domains[112,113] that lead to the formation of pores and graphene etching.[116]

Fast exfoliation of thick TMDs down to three layers was shown via UDLW.[3] Figure 5d demonstrates the ultrafast laser engineering of $MoTe_2$, where the authors designed highly ordered subwavelength nanoripples on both thick and few-layer materials and were able to thin TMD materials.[27] The authors noted that the duration of high-temperature exposure induced by the fs-laser for nanoripple formation is much shorter than the accumulated heating time caused by a CW laser, which is necessary to affect the lattice structure.

3.5. Phase Transition

Many 2D phase transitions have been studied thus far. Here, we discuss the phase transitions in graphene and TMDs initiated by fs-laser irradiation. Other strategies on phase control in TMDs were discussed elsewhere.[152,153] The most widely studied 2DM demonstrating structural phase transitions are single-layer TMDs with the chemical formula MX_2, where M stands for Mo or W and X stands for S, Se, or Te. Single-layer MX_2 materials exist in three structural forms: 2H, 1T, and 1T' (**Figure 6a**).[154] The 2H phase has a trigonal prismatic

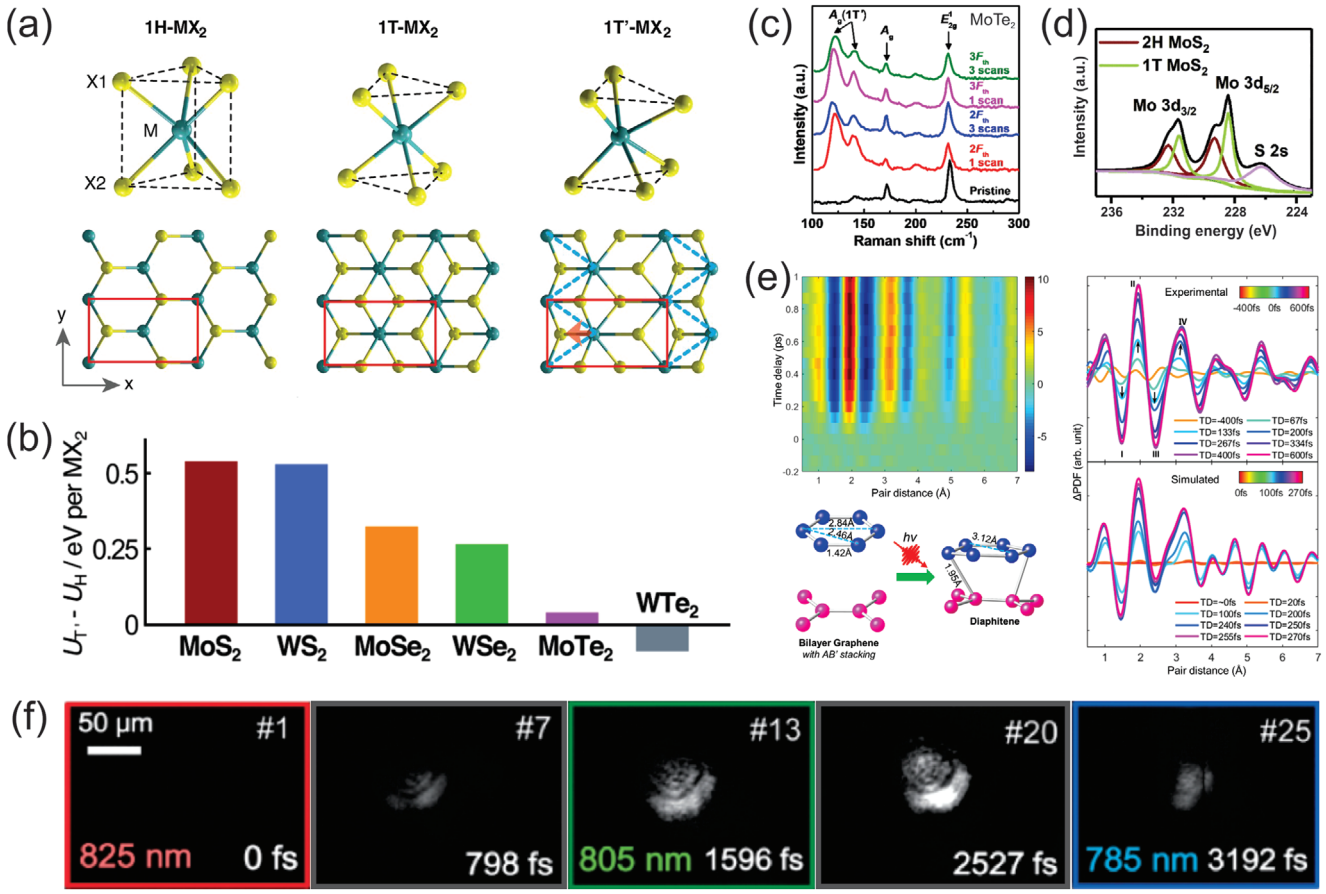

Figure 6. Phase transition in 2D materials. a) Three atomistic structures of MX_2. The red rectangles represent the unit cells. Reproduced with permission.[154] Copyright 2014, American Association for the Advancement of Science. b) Phase energy transitions between H and T' single-layer TMDs, calculated via DFT. Reproduced with permission.[157] Copyright 2016, American Chemical Society. c) Raman spectra of thick $MoTe_2$ after fs-laser irradiation with different fluences. Adapted with permission.[27] Copyright 2020, American Chemical Society. d) XPS of 1T-2H phase transition area for single-layer MoS_2 nanosheets. Reproduced with permission.[28] Copyright 2020, Elsevier. e) Experimental and simulated temporal evolution of difference pair distribution functions of twisted bilayer graphene, and the appearance of new bonds (1.95 and 3.12 A), indicating the ultrafast formation of interlayer sp^3 bonds after fs-laser illumination. Reproduced with permission.[25] Copyright 2020, American Physical Society. f) Images of the crystalline-to-amorphous phase transition in $Ge_2Sb_2Te_5$. Adapted under the terms of the CC-BY license.[162] Copyright 2017, IOP Publishing.

coordination pattern, whereas the 1T and 1T' phases have octahedral and distorted octahedral coordination patterns, respectively. In the semiconducting 2H phase, TMDs have an optical bandgap ranging from 1.0 to 2.5 eV, while there is no bandgap in the 1T phase, and the 1T' phase exhibits a small bandgap of ≈0.1 eV.[155,156] DFT calculations showed that the 2H phase is the ground-state phase of all single-layer MX_2, except for WTe_2, where the 1T' phase has the lowest energy (Figure 6b).[157] $MoTe_2$ and WTe_2 are of significant interest for phase transitions due to their small T'-2H energy difference.

Nonlinear optical imaging, thinning, and phase transition from 2H to 1T' in $MoTe_2$ were demonstrated by varying the fs-laser fluence (Figures 5d and 6c).[27] Moreover, due to the sub-picosecond timescale of the phase transition, the authors were able to fabricate a vertical junction with both 1T' and 2H phases coexisting by introducing T_e vacancies. No oxides, including TeO_2, MoO_2, and MoO_3, were detected in either the top 1T' or bottom 2H layers after the UDLW. Similar effects have been observed in other 2DM such as TMDs using photochemical etching with a CW-laser.[145] Considering that $MoTe_2$ and other TMDs demonstrate semiconducting properties, charge excitation through the bandgap is possible.[64] The lifetime of these excitations is sufficient to initiate chemical reactions with the water molecules.

The 1T to 2H phase transition was induced through IR UDLW in single-layer MoS_2 nanosheets within 800 nm thick films with submicrometer resolution.[28] This transition is irreversible and requires high energy irradiation. Figure 6d shows the XPS spectrum of the phase-transition area close to the fs-laser-irradiated area of the MoS_2 nanosheet film. The 2H phase of MoS_2 is observed only within the heat-affected zone, and the authors managed to limit it to 0.4 μm by introducing ps delays between fs-laser pulses.

Phase transitions upon ultrafast laser irradiation were also found in $TaS_{2-x}Se_x$.[158] Within a single 300 fs laser pulse, the structure of layered TMD crystals undergoes an insulator-to-metal transition, shifting from a Mott insulating state to a stable hidden charge density wave state. The appearance of the latter

state resulted in a huge resistivity drop at low temperatures and a certain laser power due to the photodoping effect. However, upon heating, the resistivity returned to that of the thermal equilibrium phase already at 120 K.

Another interesting example is the phase transition from twisted bilayer graphene to a 2D diamond-like structure induced by fs-laser irradiation (Figure 6e).[25] Using ultrafast electron diffraction, the authors found that the transition from twisted bilayer graphene to diaphitene, the 2D form of bulk diaphite,[121] occurred within 330 fs, and the structure was maintained for at least 2 ns and recovered back to graphene within 5.56 ms. However, an ultrafast structural transition from sp^2 to a mixture of sp^2 and sp^3 carbon bonds was not observed in the aligned graphene sheets. This study paves the way for the formation of stable 2D diamond and diamond thin films.[159]

Other studies on 2DM have described the phase transitions in $Ge_2Sb_2Te_5$[160,161] and Fe_3GeTe_2[162] caused by fs-laser pulses. The reversible transition from the crystalline to the amorphous phase in $Ge_2Sb_2Te_5$ occurred within only one fs pulse, which is highly desired for nonvolatile electronic memory devices.[163] $Ge_2Sb_2Te_5$ can undergo repeated phase changes between its crystalline and amorphous phases, and the transition from the crystalline to the amorphous phase was captured on a single-event basis within 800 fs (Figure 6f). Few-layered vdW Fe_3GeTe_2 2D crystals exhibit ferromagnetism at or above room temperature.[164] Irradiation with a fs-laser efficiently tunes the magnetic ordering in these crystals by optical doping and leads to the emergence of ferromagnetic order at room temperature demonstrating light-tunable magnetism in the intrinsic 2D vdW structures.[162] A laser-induced electric field can write or erase domain structures in a $LiNbO_3$ crystal with a resolution down to 20 nm, depending on the laser-writing direction.[165] This approach offers a pathway for controllable nanoscale domain engineering of $LiNbO_3$ and other transparent ferroelectric crystals and thin layers.

3.6. Doping and Energy Band Alignment

Semimetallic graphene typically can be transformed into a semiconductor via nanopatterning or growth from small molecules.[166] An energy bandgap occurs as a result of quantum confinement when the size of the graphene ribbons decreases below 10–12 nm.[167–169] Utilizing UDLW with high photon energy provides a selective approach for creating high-density, in-plane pores, and nanoribbons in monolayer graphene.[170] Pore formation was observed following the TPO process of graphene after saturation of the basal plane with sp^3-type defects (**Figure 7a**).[103] The mechanism of graphene modification by pore nucleation is similar to oxide domains growth on the energetically weakest sites of the formed graphene oxide.[112] This approach can be applied to tune the properties of graphene field-effect transistors (FET) and sensors, increasing the efficiency of signal conversion due to the presence of functional groups at the nanoribbon edges. Postannealing in an inert atmosphere can reduce the effect of oxygen groups on conductivity and mobility, restoring graphene to intrinsic conditions but with the formation of pores. The generation of nanopores and nanogaps with UDLW can be utilized for the atomic-scale ablation of 2DM. Local UDLW was used to predefine the development of the nanogaps during the electroburning process.[117] Unlike CW lasers, fs-lasers reduce the heat diffusion around the processed area, resulting in sharper patterns.

The semiconducting properties of graphene can be controlled by doping with heteroatoms, such as B and N.[171] Moreover, the dopant atoms can tune the main charge carrier type in graphene. Doping via covalent functionalization with molecules containing amino groups is possible by generating atomic vacancies followed by amino moiety oxidation.[172] Another controllable doping method for 2DM is based on light-induced isomerization of organic molecules absorbed on graphene.[173] The fast light-responsive isomerization of azobenzene chromophores within a few fs shows promising applicability for modulating doping in hybrid graphene systems.[174] It was also observed that the presence of different molecules on graphene[50] can tune the generated charge carrier dynamics due to the Fermi level shift,[42] even for physically absorbed dopants.[175] This brings the manipulation of light–matter interactions to the molecular level, opening a new era of photochemistry.

GO naturally contains a significant number of oxygen-containing defects that can be restored through proper reduction. GO is an attractive option for preparing nitrogen-doped graphene through laser-assisted methods due to the lower energy required for bond formation on these defects.[94] Figure 7b demonstrates the programmable nitrogen doping and simultaneous reduction of GO by UDLW in an NH_3 atmosphere.[171] Three types of N bonds were observed, and their formation energies were calculated as follows: graphitic-N (formation energy 0.43 eV), pyridinic-N (2.60 eV), and pyrrolic-N (7.77 eV). Since graphitic-N mainly contributes to the n-type doping of graphene,[176] adjusting the laser parameters allows precise control of the electron concentration. However, regardless of the method used to produce nitrogen-doped graphene, the presence of oxygen in air can compensate for n-type doping and even convert it to p-doping.[128,129] UDLW enhances the chemical detachment of oxygen, and the level of detached oxygen molecules can be controlled by varying the laser photon flux or the concentration of oxygen in the environment. The removal of adsorbates or polymer residues with a doping effect has also been observed with low doses of laser pulses under normal conditions.[112,177]

As discussed earlier, an ultrafast laser is an obvious tool for the exfoliation of single layers from bulk materials by ultrafast charge-induced splitting of layers.[3,27,134,149] Simultaneous exfoliation and pore formation have been demonstrated using a water-ethanol solution for graphene,[181] MoS_2, WS_2, and hBN flakes (Figure 7c).[178] The strong electric field at the laser focal point is expected to induce Coulomb repulsion,[182] breaking the bonds within the 2D flakes and solvent molecules,[183] leading to additional functionalization of the flakes and causing cracking, defect propagation, or phase transition.[184] Longer irradiation times are expected to divide the 2D sheets into multiple 2D nanoparticles (quantum dots) with sizes as small as 3 nm. A similar effect was observed for the fs-laser induced simultaneous exfoliation and pore formation in graphene in water only.[185] Notably, these effects were only visible for the ultrafast laser pulses, indicating the generation of oxidative species.[186]

The doping of TMDs induced by a fs-laser differs from that of graphene. Recently, doping with UDLW was demonstrated in MoS_2 structures.[122,180] MoS_2 is a wide bandgap semiconductor

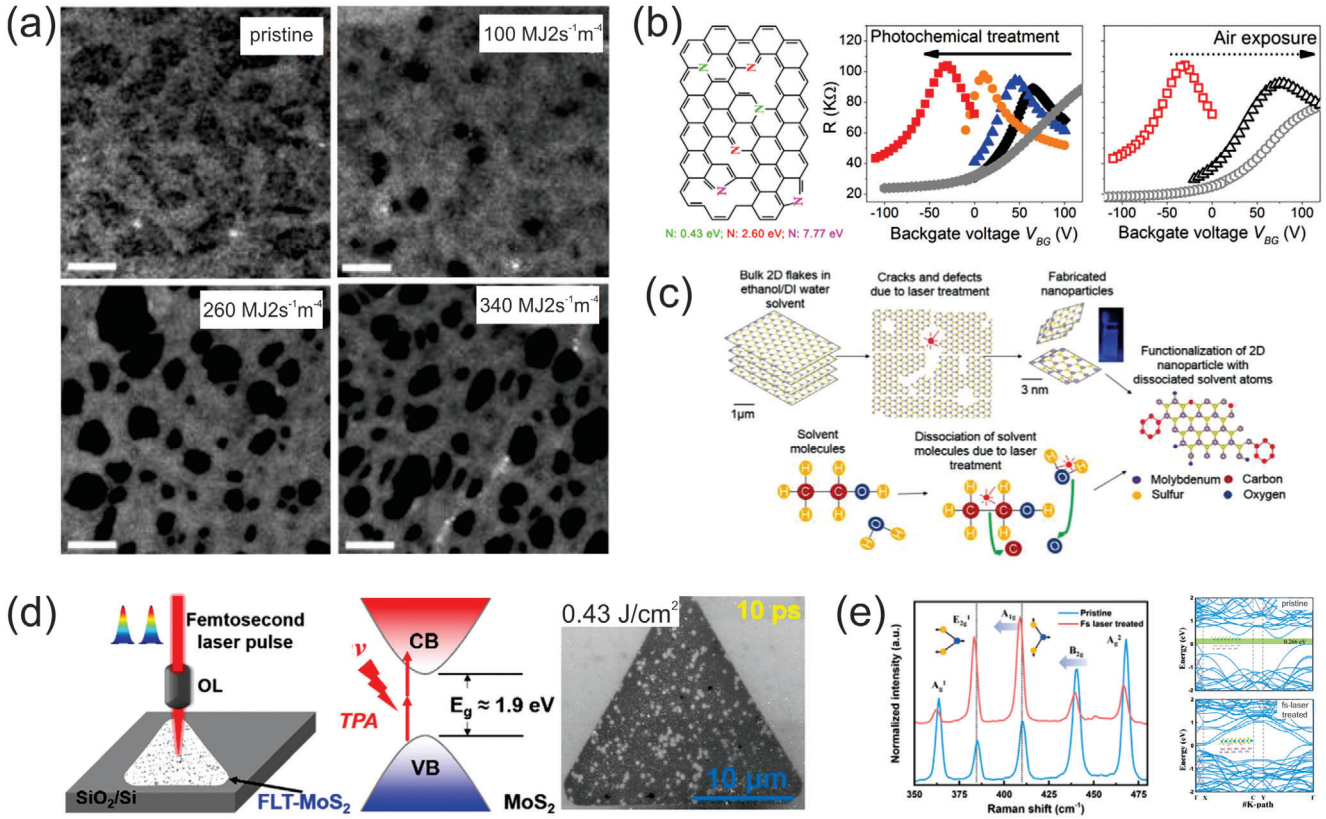

Figure 7. Femtosecond laser-induced energy alignment in 2DM. a) Pores formation in single-layer graphene during two-photon oxidation under high irradiation dose. Reproduced with permission.[103] Copyright 2019, Elsevier. b) N-doping of graphene during photochemical treatment. Adapted with permission.[128] Copyright 2017, American Chemical Society. Reproduced with permission.[171] Copyright 2013, John Wiley and Sons. c) Pores formation in MoS_2 flakes after fs-laser irradiation in water-ethanol solution. Reproduced with permission.[178] Copyright 2018, John Wiley and Sons. d) Scheme of fs-laser nanopatterning of MoS_2 flakes, their band structure, optical images after pores formation, and energy band modulation by local laser-induced removing of S atoms. Adapted with permission.[179] Copyright 2019, Royal Society of Chemistry. e) Fs-laser-controlled band alignment engineering in BP/MoS_2 heterostructures. Adapted with permission.[180] Copyright 2023, Elsevier.

with a Fermi level close to the conduction band, making it an n-type doped material. The photon energy of the typically used fs-lasers falls in the visible or near-infrared band, while the optical bandgap of monolayer MoS_2 is ≈1.9 eV. Therefore, MoS_2 can be excited and damaged by UDLW through TPA. Ultrafast laser pulses have different effects on Mo and S bonds, causing a photochemical reaction with oxygen that leads to the evaporation of sulfur-oxygen compounds and the formation of molybdenum oxide on the surface, as described by the formulas[187]

$$MoS_2 + h\nu \rightarrow Mo^{a+} + S^{b-} \quad (4)$$

$$Mo^{a+} + S^{b-} + O_2 \rightarrow MoO_3 + xMoS_3 + ySO_2 \uparrow + zSO \uparrow \quad (5)$$

The TPA of the fs-laser pulses can be responsible for generating more S vacancies on the monolayer MoS_2 and initiating chemical reactions with external molecules. The presence of S vacancies introduced additional electronic states in the energy gap, leading to a decrease of the bandgap, as shown in Figure 7d.[179] These dangling bonds are highly reactive and can form chemical bonds with oxygen atoms in air. When Mo atoms and their d-electrons are exposed to adsorbates, bonds are formed with the adsorbing species due to chemical reactions. Unsaturated Mo dangling bonds at the S-vacancy sites exhibit strong chemical reducibility and can easily reduce oxygen in air to form Mo—O bonds. Since oxygen acts as an electron acceptor, this shifts the Fermi level close to the valence band, resulting in p-type doping.

Furthermore, the last decade studies have shown that 2DM are perfect candidates for multilayer heterostructures formation without the constraint of lattice matching.[188–191] This enables ultrafast electron transfer between heterolayers,[192–195] due to substantial changes in the electronic structure of the 2D monolayers in vdW structures. Additionally, the high electron mobility within the graphene conduction band provides rapid delocalization of the transferred electrons and significantly enhances charge transport with timescales as short as sub-fs. This is a result of strong coupling at the interface of the fabricated heterojunctions.[196]

Band alignment engineering via fs-laser irradiation has been done in vdW heterostructures to enhance the charge transfer properties between the 2D layers (Figure 7e).[180] Depending on the laser irradiation fluence, this process enables precise spatial control of doping or healing effects within the heterostructure. UDLW has also been implemented for contact engineering with metal electrodes, resulting in reduced contact resistance.[122,197]

Here, we show that ultrafast laser irradiation can be utilized to change the properties of 2DM in a controllable manner compared

to CW laser illumination. Oxidation, reduction, thermoelastic modification, phase transition, and thinning precisely change the resistivity, absorbance, and band alignment in graphene and other 2DM. The large resistivity switching and stability of nanomaterials fabricated with fs-lasers are expected to have technological applications in electronic, photonic, and high-speed nonvolatile memory devices.

4. Applications of Ultrafast Laser Modified 2D Materials

In this paper, several ultrafast laser manufacturing techniques for 2DM are examined, each enabling precise, site-selective modifications with high fabrication speeds and simplified processes for various applications. These techniques, along with the mechanisms for device fabrication and their potential applications, are comprehensively evaluated and summarized in **Table 1**.

This section explores the reversible changes in the 2DM optical characteristics tuned via UDLW, allowing for optical recording and light modulation.[198,199] Recent demonstrations of photoluminescence in laser-patterned graphene and MoS_2 highlight the versatility of UDLW in controlling the optical properties of 2D materials. Ultrafast laser technologies play a pivotal role in enhancing the performance of electrical and optoelectronic devices, such as field-effect[17,101,187] and bipolar[200] transistors and photodetectors,[106,122,197] as well as providing band alignment engineering for advanced functionalities.[180] The application of UDLW extends to the development of flexible photodetectors,[201] gas sensors,[202,203] and 3D structures from 2D films,[85,204] demonstrating its broad impact on diverse fields of current research and technology development.

4.1. Photonic Devices

One of the attractive characteristics of graphene and its derivatives originates from their diverse optical properties, including fluorescence and refractive index. Reversible changes in the optical characteristics of graphene can be achieved via UDLW, opening up possibilities for optical recording and light modulation. Recently, photoluminescence (PL) of fs-laser-patterned graphene in an inert atmosphere was demonstrated.[138] PL has a maximum at 570–610 nm, depending on the laser irradiation dose, with a shift toward higher wavelengths at higher laser doses (**Figure 8a**). During UDLW, graphene was also forged. These observations are supported by the model of crystalline (quantum dots) formation due to the generation of line defects in graphene under fs-laser pulses (Figure 4d).

Similar to graphene, PL in MoS_2 can be altered by UDLW (Figure 8b). Processing with 800 nm pulses in ambient conditions resulted in an increase in PL in patterned regions,[179] while irradiation in a nitrogen atmosphere with simultaneous forging of the flake resulted in a decrease in the PL signal.[205] Therefore, it is possible to control the optical properties of 2DM by adjusting the laser parameters and the environment.

Although laser-induced periodic surface structure (LIPSS) patterning has been well-established for different materials, graphene and its composites have the potential to create unique structures with heterogeneous physical properties. An example of the practical application of the recently developed fs-laser plasmonic lithography was demonstrated in the processing of a GO film and the fabrication of micro/nanodevices with controlled optical properties (Figure 8c).[198,199] The presence of inhomogeneous dielectric permittivity within the layers of the GO material leads to a non-trivial phenomenon in the interaction between the plasmons and light. The interaction between incident light and the surface results in the excitation of transverse electric surface plasmons (TE-SPs). These TE-SPs modulate the distribution of the laser energy, resulting in LIPSS oriented parallel to the direction of the laser polarization. This unusual TE-SP wave was generated due to the gradient change in the distribution of the dielectric permittivity, extending from the surface to the inner part of the rGO/GO sample along the *z*-axis, following fs-laser irradiation. UDLW affects both the final thickness of the grooves, caused by the reorientation and reconstruction of the GO flakes, and the refractive indices at the ridge and valley positions. The spatial orientation of this grating was parallel, in contrast to the previously observed subwavelength rippling of GO during fs-laser reduction, which was perpendicular to the polarization direction.[208]

Li et al. have developed multimode optical recording and the generation of full-color 3D images in GO-dispersed polymers based on hologram-encoded refractive-index modulation by a focused fs-laser beam, as shown in Figure 8d.[206,207] This method utilizes fs-laser two-photon reduction, which induces a substantial refractive-index modulation ranging from 10^{-2} to 10^{-1}. Simultaneously, there was a decrease in fluorescence intensity, enhancing both information security and storage capacity, allowing to reach up to 290 GB per disc.[209] To further improve storage capacity, manipulation of other intrinsic optical properties, such as fluorescence emission, is possible through photoreduction.[210] Using a fs-laser with a low repetition rate and low power, in contrast to a CW laser, offers the advantages of high resolution and precise control over the fluorescence lifetimes.

UDLW was used to generate spin defects in the hBN flakes.[211,212] This method has potential applications in quantum sensors and quantum networks. The defect density was controlled by the fs-laser pulse energy, which helped reduce surface damage. While the fs-laser energy required to generate spin defects in hBN damaged the Si/SiO_2 and Au substrates, it caused minimal damage to the quartz substrate due to its low absorbance of visible and NIR photons. In addition, nano-sized bright luminescent centers can be created in hBN via UDLW,[213] allowing for single-photon emission from point defects in monolayer and few-layer hBN at room temperature.

4.2. Electrical and Optoelectronic Devices

The opening of the bandgap in graphene FETs was demonstrated by local TPO.[101] Utilizing local photochemical doping in a part of the channel in graphene FETs, in-plane junctions such as p–n[128] and p–p$^+$[106] have been successfully demonstrated (**Figure 9a**). The generation of a photocurrent at low power densities in the p–p$^+$ junctions formed in single-layer graphene was attributed to the photothermoelectric effect.

This approach is applicable to other devices based on 2DM. By combining black phosphorus (BP) and MoS_2,

Table 1. Prospective applications of ultrafast laser modified 2DM.

Application area	Structure	Fs-laser initiated fabrication mechanism	Device/ Specified usage	Performance/ functionalities	Challenges	Refs.
Electronics	Single-layer graphene	n-doping by grafted NH_2 groups	n-type FET	Reproducible n-doping in normal conditions. Low number of functional groups (only 3%)	V_{Dirac} is still in the p-type region	[17]
		TPO, p-doping with oxygen-containing groups	p-type FET	P-type performance in air, bandgap engineering	Low mobility and ON/OFF ratio	[101]
		Vacancy-type defects generation	Molecular electronics	Sharper pattern compared with CW lasers, lower current for electroburning	Size of the gaps for single molecules	[117]
	Multilayer $Ge_2Sb_2Te_5$	Phase transition	Nonvolatile memory	Sub-ps phase transition	Uniformity, thermal effects	[160,161]
	BP/MoS_2 heterostructure	Band alignment engineering	Ternary inverter	Wide output swing with 3 logic states, the V_{Gain} of 0.35	Long-term stability	[180]
	Multilayer MoS_2	Ablation	n-type and p-type FET	Nanoribbon arrays, high ON/OFF ratio	Control of nanoribbon size, mobility	[187]
Opto-electronics	Single-layer graphene	TPO, thermoelectric effect	Photodetector, p–p^+ junction	Responsivity of 100 mA W^{-1}, noise equivalent power ≈6 kW cm^{-2}, low operational voltage	Mobility, relatively wide junction area	[106]
	Multilayer MoS_2	Contact engineering	Phototransistor	High rectification and ON/OFF ratio of 10^4, improved contact resistance	Operational light power range, dark current	[122]
			Photodetector	Responsivity of 1.72 A W^{-1}, rectification ratio $>10^4$, detectivity of 1.8 10^{13} Jones	Fill factor, domination of space charge limited current	[197]
	BP/MoS_2 heterostructure	Band alignment engineering	Broad range photodetector	Responsivity of 64.5 A W^{-1}, detectivity of ≈1.48 10^{11} Jones.	Complexity in fabrication, reproducibility	[180]
			Bipolar junction transistor, phototransistor	Rectification ratio of 10^3 and responsivity of 2.2 A W^{-1}	Wide base, responsivity of the phototransistor	[200]
	rGO–ZnO	DLW on a flexible substrate	UV photodetector	Responsivity of 3.24 A W^{-1}. Intact substrate	Response times, responsivity	[201]
	Multilayer SnSe	Ablation, LIPPS, thermoelectric effect	Integrated photodetector	Self-powered, responsivity of 4 mV W^{-1} in NIR region	Response times, detectivity	[214]
	CuO/MoS_2 heterostructure	Contact engineering in hBN protected environment	Broad range photodetector	High responsivity of 250 A W^{-1} and detectivity of 6.5 10^{11} Jones, long-time stability	Operational voltage, rectification factor	[215]
Photonics	Single-layer graphene	Inert atmosphere forging	LED and display	High PL with a maximum at 600 nm	Polymer residues	[138]
	Single-layer MoS_2		MEMS in photonic circuits, optical recording	PL quenching, longer fluorescence lifetime	Atmosphere control	[205]
	rGO-polymer	Reduction, refractive-index modulation	Multimode optical recording, holograms	Generation of 2D and 3D color images and holograms	Pixel size, viewing angle	[206,207]
	Monolayer and multilayer hBN	Ablation, phase change from hBN to cBN	Laser or LED, single photon emitters	Localized single photon emission centers with $g^2(0)$ ≈0.2 and a line width of 1.4 nm	Substrate damage	[213]

(*Continued*)

Table 1. (Continued)

Application area	Structure	Fs-laser initiated fabrication mechanism	Device/ Specified usage	Performance/ functionalities	Challenges	Refs.
	Graphene- InAs/GaAs QDs	DLW followed by ns-laser irradiation	Laser, saturable absorber	Single pulse energy of 0.33 nJ and a pulse width of 483 fs, fast carrier recovery times	Long-term stability	[241]
Spintronics	Few-layer Fe_3GeTe_2	Tune of the magnetic ordering by optical doping	Storage, magnetic sensor	Magnetic anisotropy energy and T_{Curie} modulation	Stability of ferromagnetism in room T	[162]
	Multilayer hBN	Ablation, generation of B vacancies	Quantum sensors	Stable PL from generated defects, high magnetic resonance contrast. Single photon emission centers with $g^2(0) \approx 0.34$	Substrate damage, control of PL, and type of defects	[211, 212]
Plasmonics	rGO	Lithography (cylindrical focusing), LIPPS	Polarization-dependent devices	Optical birefringence (≈0.18), anisotropic photoresponse (≈1.21 and ≈0.46 ratio) in the visible range	Control of anisotropy	[198,199]
	Single-layer graphene	Inert atmosphere forging	Resonators, sensors	Guiding surface plasmons via local strain engineering	Homogeneous elevation in forged areas	[136]
		Ablation, LIPPS		Local anisotropic and periodic doping of patterned areas	Resolution, variation in doping level	[237]
Sensors	Single-layer graphene	TPO	pH sensor	Different defect concentrations allow for sensitivity tuning, sensitivity up to 25 mV pH^{-1}	Sensitivity, high pH, polymer residues	[177]
			Biosensor and bio-interface	Enzyme activity control via oxidation level and area localization	Stability and reproducibility of enzyme activity	[222]
	Single-layer MoS_2	S vacancies generation	Molecular detection	Surface-enhanced-Raman-scattering enhancement up to 6 times, biocompatible	Enhancement factor compared with metal nanoparticles	[179]
	rGO, MoS_2, WS_2	DLW in solution	Gas sensor	Membrane surface stress sensor enhanced sensitivity and selectivity	Compensation for humidity response	[202]
	Few-layer WS_2	Phase engineering, S vacancies generation	Gas sensor	Detection limit below 0.1 ppm, response/recovery time of 43/67 s at room T	Selectivity toward NH_3	[203]
Microscale systems	rGO	Reduction on a flexible substrate, forging	Microfluidics with built-in electrodes	Resistance of 200 Ω sq^{-1}, forging up to 40 µm in height	Thermal nature of forging	[85]
		Reduction	Microjet engine, MEMS	No toxic materials, operation on a dry glass surface	Contamination	[204]
	Single-layer graphene	Inert atmosphere forging of 2D graphene into 3D shapes	MEMS, microfluidics, optomechanical resonator, 3D scaffolds	Bending stiffness is enhanced by up to five orders of magnitude	Nature of forging mechanism, control the type of defects, reproducibility	[137,140]
	GO/hydrogel	Two-photon polymerization	MEMS, 3D scaffolds	Nanofilament with a diameter of 100 nm and aspect ratio of up to 100	Low conductivity, uniformity of dispersion, biocompatibility	[223]

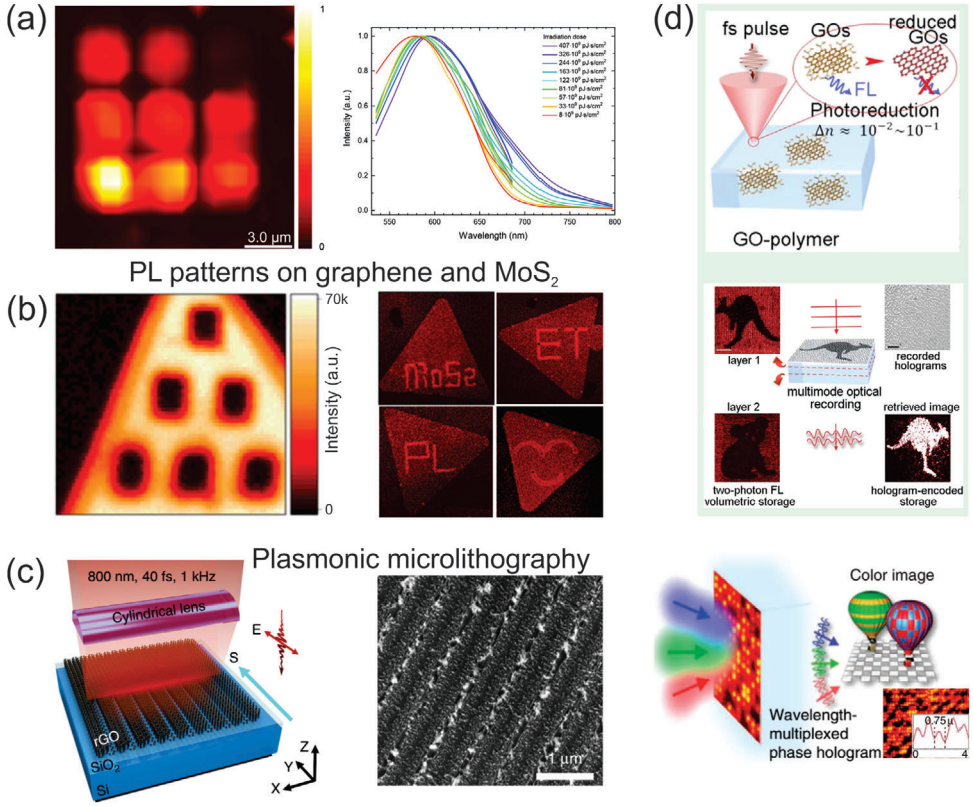

Figure 8. Ultrafast optical recording in 2D materials. a) Photoluminescent graphene patterns via fs-laser local processing. Reproduced with permission.[138] Copyright 2020, American Chemical Society. b) Photoluminescence tuning in MoS_2 by UDLW. Reproduced with permission.[179] Copyright 2019, Royal Society of Chemistry. Reproduced with permission.[205] Copyright 2021, John Wiley and Sons. c) Fs plasmonic lithography for high-speed micro/nanograting processing of GO film. Reproduced under the terms of the CC-BY license.[198] Copyright 2020, Springer Nature. d) Fs-laser two-photon reduction induced giant refractive-index modulation in GO-polymer composite and an example of recorded wavelength-multiplexed phase hologram. Adapted under the terms of the CC-BY license.[206] Copyright 2013, Springer Nature. Adapted under the terms of the CC-BY license.[207] Copyright 2015, Springer Nature.

a symmetric bipolar junction transistor was designed (Figure 9b).[200] It also performed as a gate-tunable phototransistor demonstrating high photodetectivity and photocurrent gain of $\beta \approx 21$. Moreover, for bi-component layered materials such as TMD, this method can provide an additional degree of freedom by varying the concentration of its components.

The fs-laser-induced photochemical process, in combination with the interaction of photons with surface plasmons, can result in LIPSS lithography, creating subwavelength channels in MoS_2 flakes and developing transistors with tuned doping levels (Figure 9c).[187] Chemical doping in multilayer MoS_2 occurs on both the surface and side walls of the formed nanoribbons, resulting in a clear change in the sign of the main charge carriers, along with a decrease in the total resistance and charge carrier mobility. Yan et al. fabricated self-powered SnSe photodetectors utilizing a similar approach.[214] Fabricating a LIPSS on half of the SnSe film enhanced optical absorption by 20% and generated a voltage upon illumination via a photothermoelectric effect.

UDLW has been used as a contact engineering method to enhance the photoresponse in hBN-encapsulated CuO/MoS_2 vdW heterojunctions.[215] Irradiation of MoS_2 on top of Au significantly improved the electrical resistance and resulted in Schottky contact.[122,197] This enhanced the photoresponse of the MoS_2 photodetector devices up to 1.7 A W^{-1} (Figure 9d).

UDLW was also utilized in band alignment engineering to create high-performance photodetectors and multivalued logic circuits based on BP/MoS_2 heterojunction FET.[180] Tuning the heterojunction band profile not only increased the photoresponse but also reduced the saturation limit of the incident light power (Figure 9e). The short duration of the fs-laser pulses allowed selective local doping of the heterojunction for the development of a ternary inverter (Figure 9f). To protect the devices from electrical depletion by gas molecules such as O_2 and H_2O, laser processing was performed after hBN encapsulation, which significantly improved device stability and lifetime. Decreasing the fs-laser beam spot, for example, using scanning near-field optical microscopy, can further enhance the photoresponse of 2DM photodetectors by enhancing the effective charge separation at the junction.

An et al. fabricated a flexible photodetector for UV light, by combining rGO nanoflakes with ZnO nanoparticles via single-step selective fs-laser patterning by tuning the incident photon energy in different regions of the device.[201] The device

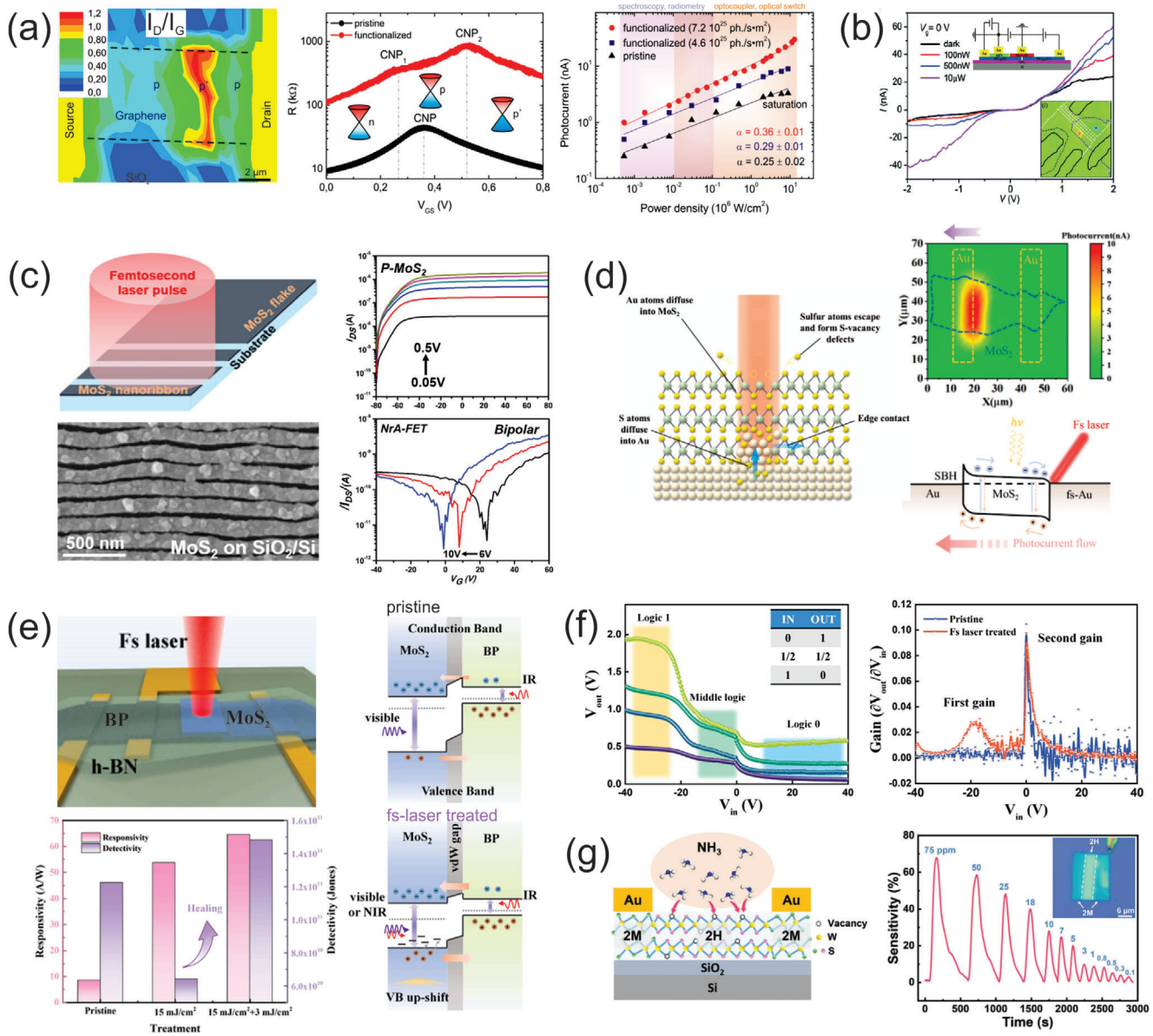

Figure 9. Ultrafast laser-induced doping of graphene, GO and other 2D materials. a) TPO of graphene channel in FET configuration with formation of a local p^+ channel and double charge neutrality point (CNP) in transfer *I–V* curves. Adapted with permission.[106] Copyright 2018, American Chemical Society. b) Gate-tunable symmetric bipolar junction transistor enabled by fs-laser irradiation of BP and MoS_2. Adapted under the terms of the CC-BY license.[200] Copyright 2020, Royal Society of Chemistry. c) Femtosecond laser induced conversion of initial *n*-doping of pristine MoS_2 flake (P-MoS_2) to *p* doping during nanoribbon array formation (NrA-FET). Adapted with permission.[187] Copyright 2019, American Chemical Society. d) Contact engineering in MoS_2 and Au interface by UDLW for asymmetric Schottky contacts. Adapted with permission.[197] Copyright 2023, Elsevier. e) The band diagrams for pristine and treated HJ devices and their time-resolved photoresponse at various gate voltages. Adapted with permission.[180] Copyright 2023, Elsevier. f) Multivalued logic on BP/MoS_2 heterojunction FET. Adapted with permission.[180] Copyright 2023, Elsevier. g) Ammonia gas sensor based on fs-laser modified few-layer WS_2 flake with 2H and 2M junctions. Adapted with permission.[203] Copyright 2023, John Wiley and Sons.

showed a high, linear, and reproducible response, and exhibited superior mechanical robustness that is useful for wearable electronics.

UDLW can enhance the sensing properties of 2DM.[216] The attachment of hydroxyl and epoxy groups to the graphene surface via the fs-laser under ambient conditions increased the sensitivity of graphene FETs to pH.[177] UDLW graphene with various pattern arrays enabled multifunctional sensing selectivity for strain, temperature, and gas detection in wearable sensors.[217] Piezoresistive membrane gas sensors for various volatile organic compounds were demonstrated by inducing defects in GO, MoS_2, and WS_2 flakes by fs-laser processing in different solutions.[202] Precise control of the fs-laser-driven phase transition in the few-layer WS_2 demonstrated the generation of a 2H-WS_2 region rich in sulfur vacancies, allowing sub-ppm ammonia detection (Figure 9g).[203]

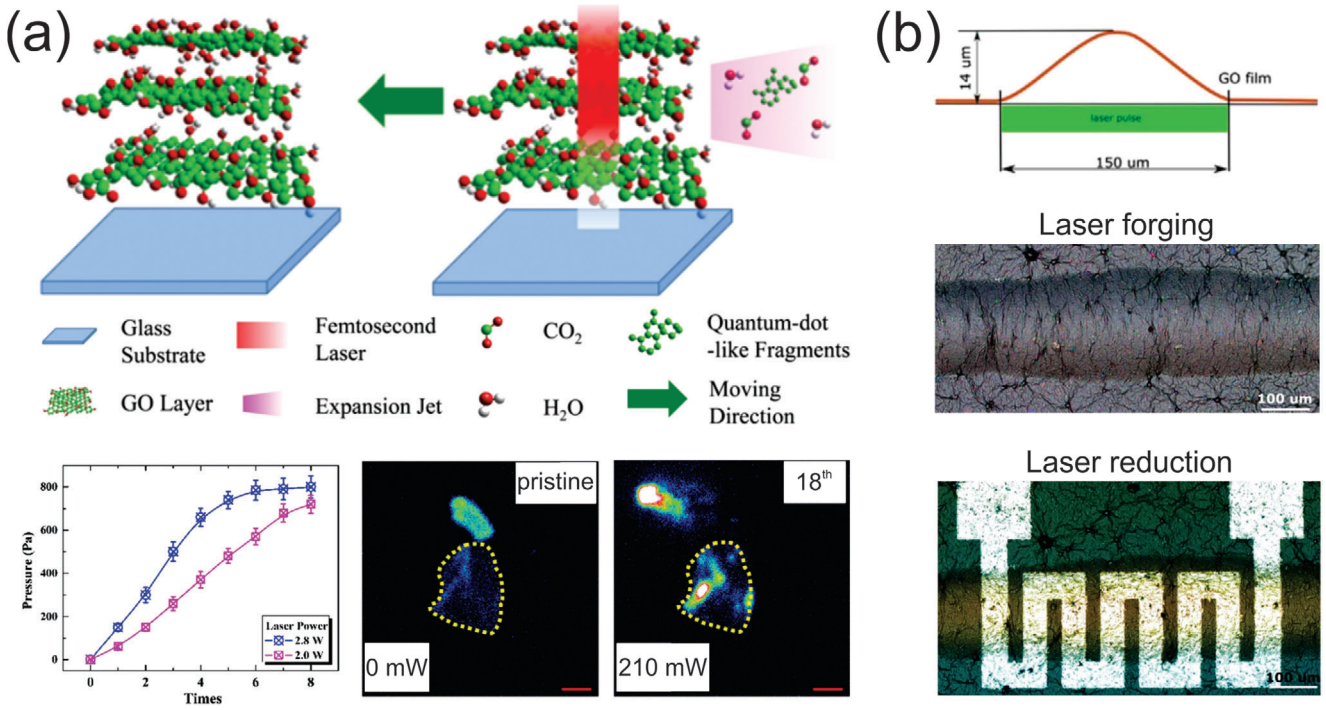

Figure 10. Ultrafast laser induced mechanical manipulation of GO. a) Laser-driven propulsion of multilayer GO flakes under multiple pulses irradiation. Adapted with permission.[204] Copyright 2018, Royal Society of Chemistry. b) GO forging and local reduction by ultrafast pulsed laser irradiation from backside and topside respectively. Adapted with permission.[85] Copyright 2017, Elsevier.

4.3. Microscale Systems

The observed explosion in GO during UDLW, involving the rapid evaporation of H_2O, CO_2, and CO groups during reduction,[19,85] can be utilized for micromotor development in light-driven micromachines[204] or 3D patterning of GO structures.[85] Upon laser irradiation, the GO layers underwent photoreduction and produced gases isotropically ejected into the atmosphere. However, the intermediate layers experienced photoreduction, with gases ejected from the side edge, creating a directional force on the GO flake. The ejected gases and quantum-dot-like fragments generated a recoiling force, moving the GO flake in the opposite direction (**Figure 10a**).[204] The pressure of the produced gases varied with the time and power of the fs-laser irradiation. Due to a certain amount of oxygen groups, the pressure is limited and suitable for small particles, providing specific delivery when GO is used as a container. The effect of local forging of graphene under ultrafast laser irradiation, based on local gas evaporation, facilitates the creation of curved structures on top of flexible substrates (Figure 10b).[85] Furthermore, these patterns can be reduced to build conductive structures on curved surfaces, which can be utilized in microfluidic applications with integrated sensors.

5. Perspectives

Traditional microfabrication processes are still actively used for the modification of 2DM properties and their integration into functional devices due to the robustness and scalability of the technology. UDLW has become a novel technological tool, providing on-demand material manipulation with less harsh environmental effects and material waste. Recent findings have progressively enhanced the efficiency of ultrafast laser processing in terms of resolution and processing speed, bringing it to a level comparable to traditional processes. Specific focusing methods allow UDLW to achieve resolution down to 10 nm.[218–220] Moreover, with the evolution of laser processing tools, the speed of the process is no longer a limitation for industrial applications. The use of microlens arrays[221] and high-speed scanning systems (galvoscanners with a speed up to 10 m s^{-1} or polygonal scanners up to km s^{-1})[22,222] provides surface treatment times comparable to those in the industry.

The development of biomaterials for sensor applications, drug delivery, and tissue engineering can be revolutionized by integrating ultrafast processing of carbon nanomaterials and DLW of biopolymers.[223,224] This involves simultaneous laser 3D structuring, reduction, or functionalization of graphene and GO. Moreover, innovative photochemical methods can covalently bind bio- and organic molecules to 2DM, paving the way for the development of functional nanorobots for theranostic applications. Recent advanced techniques, such as azide photochemistry, have been proposed to covalently modify carbon nanotubes and graphene.[225,226] This technique offers a new level of control over molecular orientation and tuning of nanomaterial properties, when combined with the genetic encoding of bioreceptors.[227] Noncovalent immobilization of proteins can be realized via the TPO of graphene with a high resolution.[228] UDLW can bring an additional level of localization and multiplexing for various bioreceptors on a single device. Practical implementation of these effects could lead to the creation of innovative

biosensors and biorobots,[229] utilizing all-optical methods for modifying structures and creating new hybrid nanoparticles.[227]

UDLW has accelerated the development of optoelectronic devices and NEMS systems based on 2DM. Modification of free-standing 2D structures is a promising direction for maskless technologies, providing 3D processing that traditional photolithography cannot achieve. Fs-laser irradiation of graphene oxide led to the creation of IR detectors based on rGO.[198] However, the performance of such devices is limited due to the presence of surface traps. Currently, ion-beam technologies are utilized for suspended graphene modification, but they also have limitations such as sample preparation, processing speed, and potential introduction of defects.[230]

Recent research on semiconducting epigraphene, covalently bonded to silicon carbide substrates, reveals a bandgap of 0.6 eV and estimated room temperature mobilities up to 5500 $cm^2\ V^{-1}\ s^{-1}$, achieved through quasiequilibrium annealing.[231] UDLW offers precise tuning of the graphene bandgap by inducing mixed sp^2 and sp^3 bonds in twisted graphene systems,[25] paving the way for the utilization of graphene with engineered optical and electronic properties for various applications. TPO of graphene promotes the area-selective atomic layer deposition in predefined areas with a resolution down to 300 nm,[232] which can be applied during the fabrication of 2DM FETs to minimize interface traps and decrease the contact resistance by tuning the Fermi level with an ultrafast laser.[233] The resolution of TPO can be further reduced by utilizing near-field effects or orthogonally polarized beams.[220] Fs-laser patterning can create 3D-shaped nanodevices with a controlled bandgap and high-speed photodetectors sensitive to light polarization.[199] Photoelastic modification of 2DM in suspended structures[140] can be utilized for novel NEMS where local stress is tunable through laser irradiation. 3D reconstruction enables the formation of electronic elements, providing control over the optical and electrical properties through nano-origami.[234,235] Local 3D reconstruction of graphene can be utilized to create flat bands, inducing superconductivity, without relying on "magic" angles in 2DM.[236]

Simultaneous modification of the mechanical and chemical properties of free-standing structures is complex and involves electron heating and relaxation on optical and acoustic phonons. Controlling the spatial arrangement of 2D materials enables the formation of folding structures to encapsulate various molecules, paving the way for submicroreactors and tubistors. UDLW reduces substrate effects and enhances the development of high-speed optical photodetectors and ultrasensitive biochemical sensors. Ultrafast laser local engineering of mechanical stress centers in graphene offers a technique that does not require specially prepared substrates.[237] Although heating effects in substrates are minimized with ultrafast lasers, it is important to consider potential factors such as light interference or the relaxation of optical phonons, which may influence the increase of light power delivered to 2DM or affect photoacoustic interactions, respectively. A proper understanding of these mechanisms is crucial for the development of ultrafast laser processing tools.

Recently, interest has shifted from 2DM to vdW structures,[238–240] creating a synergetic effect that underpins new physics. Traditional lithography techniques are ineffective for exploiting the properties of such structures due to a lack of control over the geometric orientation, doping levels, and defect introduction. Laser-based methods offer the potential to develop a time- and space-controlled process for creating self-aligned channels in vdW transistors with controlled anisotropy of properties.[200,241]

Local laser-enabled modification of one layer in the vdW structure allows tuning of the energy gap and electronic profile via all-optical methods for integrated circuit development.[180,242] Different relaxation processes in graphene and TMD structures after ultrafast excitation can be utilized for the separate modification of various vdW layers. Combining selective laser-induced ablation and doping enables the formation of self-limited heterojunctions in the layered structures.

6. Conclusion

Ultrafast laser processing is an emerging tool for the modification of materials with improved functional properties. This technology is currently evolving from a laboratory concept to a practical manufacturing tool. Working at the atomic scale and enabling processes such as reduction, doping, exfoliation, and functionalization of 2DM via ultrafast laser processing offers a novel and rapid approach to manipulate and tailor these materials for future applications. This method not only enhances 2DM properties but also incorporates environmentally sustainable practices by minimizing thermal damage and reducing chemical waste.

The high spatial and time-resolved control of the fundamental properties of 2DM achieved by ultrafast lasers holds great promise for the 3D manipulation and modification of nanomaterials, challenging conventional microfabrication methods. Integration with biopolymer structures for sensing, imaging, and theranostic applications and processing speeds using galvoscanners, comparable to traditional lithography, highlights the potential of ultrafast laser processing to revolutionize material sciences. As 2D materials continue to unveil new areas of application and exhibit extraordinary properties, UDLW accelerates the development of custom-oriented applications.

All-optical processing technologies for creating hybrid systems based on 2D materials, combining physical channel patterning with control of their properties, are on the horizon. This paves the way for the design of photonic, electrical, optoelectronic devices, and sensors based on hybrid graphene and other 2DM nanostructures that operate on new physical principles and possess biomimicking properties.

Acknowledgements

A.V.E. and M.P. acknowledged the Jane and Aatos Erkko Foundation for support. I.I.B. acknowledged the ANTARES project that has received funding from the European Union's Horizon 2020 research and innovation programm under Grant Agreement SGA-CSA No. 739570 under FPA No. 664387 (doi.org/10.3030/739570).

Conflict of Interest

The authors declare no conflict of interest.

Keywords

2D materials, atomic reconstruction, charge carrier dynamics, femtosecond laser, graphene, multiphoton process, transition metal dichalcogenide

Received: February 26, 2024
Revised: April 23, 2024
Published online:

[1] M. Malinauskas, A. Žukauskas, S. Hasegawa, Y. Hayasaki, V. Mizeikis, R. Buividas, S. Juodkazis, *Light: Sci. Appl.* **2016**, *5*, e16133.
[2] D. M. A. Mackenzie, J. D. Buron, P. R. Whelan, B. S. Jessen, A. Silajdźić, A. Pesquera, A. Centeno, A. Zurutuza, P. Bøggild, D. H. Petersen, *2D Mater.* **2015**, *2*, 045003.
[3] S. J. An, Y. H. Kim, C. Lee, D. Y. Park, M. S. Jeong, *Sci. Rep.* **2018**, *8*, 12957.
[4] P. Kumar, L. S. Panchakarla, C. N. R. Rao, *Nanoscale* **2011**, *3*, 2127.
[5] J. Lin, Z. Peng, Y. Liu, F. Ruiz-Zepeda, R. Ye, E. L. G. Samuel, M. J. Yacaman, B. I. Yakobson, J. M. Tour, *Nat. Commun.* **2014**, *5*, 5714.
[6] Y. Xu, B. Jiao, Y. Wang, S. Xue, H. Gao, K. Yu, X. Fan, Y. Liu, Y. Tao, L. Deng, W. Xiong, *ACS Appl. Mater. Interfaces* **2022**, *14*, 5558.
[7] D. A. Sokolov, C. M. Rouleau, D. B. Geohegan, T. M. Orlando, *Carbon* **2013**, *53*, 81.
[8] P. Kumar, *RSC Adv.* **2013**, *3*, 11987.
[9] P. S. Kollipara, J. Li, Y. Zheng, *Research* **2020**, *2020*, 6581250.
[10] B. W. Su, X. L. Zhang, W. Xin, H. W. Guo, Y. Z. Zhang, Z. B. Liu, J. G. Tian, *J. Mater. Chem. C: Mater.* **2021**, *9*, 2599.
[11] S.-T. M. Akkanen, H. A. Fernandez, Z. Sun, S.-T. M. Akkanen, H. A. Fernandez, Z. Sun, *Adv. Mater.* **2022**, *34*, 2110152.
[12] R. You, Y. Q. Liu, Y. L. Hao, D. D. Han, Y. L. Zhang, Z. You, *Adv. Mater.* **2020**, *32*, 1901981.
[13] J.-H. Yoo, E. Kim, D. J. Hwang, *MRS Bull.* **2016**, *41*, 1002.
[14] H. Ohnishi, E. Inami, J. Kanasaki, *Surf. Sci.* **2011**, *605*, 1497.
[15] R. J. Stöhr, R. Kolesov, K. Xia, J. Wrachtrup, *ACS Nano* **2011**, *5*, 5141.
[16] Z. Lin, H. Liu, L. Ji, W. Lin, M. Hong, *Nano Lett.* **2020**, *20*, 4947.
[17] Y. Xu, J. Jin, W. Wang, Z. Peng, H. Liu, Y. Wang, Z. Wei, J. You, J. Impundu, L. Sun, H. Wei, Y. Jun Li, M. Xue, *Mater. Lett.* **2023**, *350*, 134979.
[18] H. Liu, S. Ryu, Z. Chen, M. L. Steigerwald, C. Nuckolls, L. E. Brus, *J. Am. Chem. Soc.* **2009**, *131*, 17099.
[19] R. Trusovas, K. Ratautas, G. Račiukaitis, J. Barkauskas, I. Stankevičienė, G. Niaura, R. Mažeikienė, *Carbon* **2013**, *52*, 574.
[20] R. Sahin, E. Simsek, S. Akturk, *Appl. Phys. Lett.* **2014**, *104*, 053118.
[21] B. Senyuk, N. Behabtu, A. Martinez, T. Lee, D. E. Tsentalovich, G. Ceriotti, J. M. Tour, M. Pasquali, I. I. Smalyukh, *Nat. Commun.* **2015**, *6*, 7157.
[22] A. Enrico, O. Hartwig, N. Dominik, A. Quellmalz, K. B. Gylfason, G. S. Duesberg, F. Niklaus, G. Stemme, *ACS Nano* **2023**, *17*, 8041.
[23] J. Ha, H. Y. Jung, J. Hao, B. Li, A. Raeliarijaona, J. Alarcón, H. Terrones, P. M. Ajayan, Y. J. Jung, J. Kim, D. Kim, *Nanoscale* **2017**, *9*, 16627.
[24] J. Zhang, R. Wang, X. Zhu, A. Pan, C. Han, X. Li, Dan Zhao, C. Ma, W. Wang, H. Su, C. Niu, *Nat. Commun.* **2017**, *8*, 683.
[25] D. Luo, D. Hui, B. Wen, R. Li, J. Yang, X. Shen, A. H. Reid, S. Weathersby, M. E. Kozina, S. Park, Y. Ren, T. D. Loeffler, S. K. R. S. Sankaranarayanan, M. K. Y. Chan, X. Wang, J. Tian, I. Arslan, X. Wang, T. Rajh, J. Wen, *Phys. Rev. B* **2020**, *102*, 155431.
[26] S. Ideta, D. Zhang, A. G. Dijkstra, S. Artyukhin, S. Keskin, R. Cingolani, T. Shimojima, K. Ishizaka, H. Ishii, K. Kudo, M. Nohara, R. J. D. Miller, *Sci. Adv.* **2018**, *4*, eaar3867.
[27] M. Wang, D. Li, K. Liu, Q. Guo, S. Wang, X. Li, *ACS Nano* **2020**, *14*, 11169.
[28] C. Xu, L. Jiang, X. Li, C. Li, C. Shao, P. Zuo, M. Liang, L. Qu, T. Cui, *Nano Energy* **2020**, *67*, 104260.
[29] Y. Tan, F. Luo, M. Zhu, X. Xu, Y. Ye, B. Li, G. Wang, W. Luo, X. Zheng, N. Wu, Y. Yu, S. Qin, X. A. Zhang, *Nanoscale* **2018**, *10*, 19964.
[30] M. Z. Iqbal, M. W. Iqbal, M. F. Khan, J. Eom, *Phys. Chem. Chem. Phys.* **2015**, *17*, 20551.
[31] A. V. Emelianov, D. Kireev, D. D. Levin, I. I. Bobrinetskiy, *Appl. Phys. Lett.* **2016**, *109*, 173101.
[32] D. A. Bandurin, D. Svintsov, I. Gayduchenko, S. G. Xu, A. Principi, M. Moskotin, I. Tretyakov, D. Yagodkin, S. Zhukov, T. Taniguchi, K. Watanabe, I. V. Grigorieva, M. Polini, G. N. Goltsman, A. K. Geim, G. Fedorov, *Nat. Commun.* **2018**, *9*, 5392.
[33] J. M. Dawlaty, S. Shivaraman, M. Chandrashekhar, F. Rana, M. G. Spencer, *Appl. Phys. Lett.* **2008**, *92*, 042116.
[34] L. M. Malard, K. Fai Mak, A. H. Castro Neto, N. M. R. Peres, T. F. Heinz, *New J. Phys.* **2013**, *15*, 015009.
[35] D. Sun, G. Aivazian, A. M. Jones, J. S. Ross, W. Yao, D. Cobden, X. Xu, *Nat. Nanotechnol.* **2012**, *7*, 114.
[36] K. Chen, M. N. Yogeesh, Y. Huang, S. Zhang, F. He, X. Meng, S. Fang, N. Sheehan, T. H. Tao, S. R. Bank, J.-F. Lin, D. Akinwande, P. Sutter, T. Lai, Y. Wang, *Carbon* **2016**, *107*, 233.
[37] I. Gierz, J. C. Petersen, M. Mitrano, C. Cacho, I. C. E. Turcu, E. Springate, A. Stöhr, A. Köhler, U. Starke, A. Cavalleri, *Nat. Mater.* **2013**, *12*, 1119.
[38] J. C. Johannsen, S. Ulstrup, F. Cilento, A. Crepaldi, M. Zacchigna, C. Cacho, I. C. E. Turcu, E. Springate, F. Fromm, C. Raidel, T. Seyller, F. Parmigiani, M. Grioni, P. Hofmann, *Phys. Rev. Lett.* **2013**, *111*, 027403.
[39] G. Jnawali, Y. Rao, H. Yan, T. F. Heinz, *Nano Lett.* **2013**, *13*, 524.
[40] K. J. Tielrooij, J. C. W. Song, S. A. Jensen, A. Centeno, A. Pesquera, A. Zurutuza Elorza, M. Bonn, L. S. Levitov, F. H. L. Koppens, *Nat. Phys.* **2013**, *9*, 248.
[41] J. C. W. Song, L. S. Levitov, *J. Phys. Condens. Matter* **2015**, *27*, 164201.
[42] A. Tomadin, S. M. Hornett, H. I. Wang, E. M. Alexeev, A. Candini, C. Coletti, D. Turchinovich, M. Kläui, M. Bonn, F. H. L. Koppens, E. Hendry, M. Polini, K.-J. Tielrooij, *Sci. Adv.* **2018**, *4*, eaar5313.
[43] H. Wang, J. H. Strait, P. A. George, S. Shivaraman, V. B. Shields, M. Chandrashekhar, J. Hwang, F. Rana, M. G. Spencer, C. S. Ruiz-Vargas, J. Park, *Appl. Phys. Lett.* **2010**, *96*, 081917.
[44] M. M. Jadidi, R. J. Suess, C. Tan, X. Cai, K. Watanabe, T. Taniguchi, A. B. Sushkov, M. Mittendorff, J. Hone, H. D. Drew, M. S. Fuhrer, T. E. Murphy, *Phys. Rev. Lett.* **2016**, *117*, 257401.
[45] K. F. Mak, J. Shan, T. F. Heinz, *Phys. Rev. Lett.* **2011**, *106*, 046401.
[46] S. Winnerl, M. Mittendorff, J. C. König-Otto, H. Schneider, M. Helm, T. Winzer, A. Knorr, E. Malic, *Ann. Phys.* **2017**, *529*, 1700022.
[47] P. A. George, J. Strait, J. Dawlaty, S. Shivaraman, M. Chandrashekhar, F. Rana, M. G. Spencer, *Nano Lett.* **2008**, *8*, 4248.
[48] A. Rustagi, C. J. Stanton, *Phys. Rev. B* **2016**, *94*, 195207.
[49] S. Tani, F. Blanchard, K. Tanaka, *Phys. Rev. Lett.* **2012**, *109*, 166603.
[50] Z. Zhang, T. Lin, X. Xing, X. Lin, X. Meng, Z. Cheng, Z. Jin, G. Ma, *Appl. Phys. Lett.* **2017**, *110*, 111108.
[51] A. Tomadin, D. Brida, G. Cerullo, A. C. Ferrari, M. Polini, *Phys. Rev. B* **2013**, *88*, 035430.
[52] C. H. Lui, K. F. Mak, J. Shan, T. F. Heinz, *Phys. Rev. Lett.* **2010**, *105*, 127404.
[53] S. Butscher, F. Milde, M. Hirtschulz, E. Malić, A. Knorr, *Appl. Phys. Lett.* **2007**, *91*, 203103.
[54] Q. Ma, N. M. Gabor, T. I. Andersen, N. L. Nair, K. Watanabe, T. Taniguchi, P. Jarillo-Herrero, *Phys. Rev. Lett.* **2014**, *112*, 247401.
[55] M. W. Graham, S.-F. Shi, Z. Wang, D. C. Ralph, J. Park, P. L. McEuen, *Nano Lett.* **2013**, *13*, 5497.

[56] M. W. Graham, S.-F. Shi, D. C. Ralph, J. Park, P. L. McEuen, *Nat. Phys.* **2013**, *9*, 103.
[57] R. Bistritzer, A. H. MacDonald, *Phys. Rev. Lett.* **2009**, *102*, 206410.
[58] L. Huang, B. Gao, G. Hartland, M. Kelly, H. Xing, *Surf. Sci.* **2011**, *605*, 1657.
[59] J. M. Iglesias, M. J. Martín, E. Pascual, R. Rengel, *Appl. Phys. Lett.* **2016**, *108*, 043105.
[60] A. J. Frenzel, C. H. Lui, Y. C. Shin, J. Kong, N. Gedik, *Phys. Rev. Lett.* **2014**, *113*, 056602.
[61] D. Sun, Z.-K. Wu, C. Divin, X. Li, C. Berger, W. A. de Heer, P. N. First, T. B. Norris, *Phys. Rev. Lett.* **2008**, *101*, 157402.
[62] S. A. Jensen, Z. Mics, I. Ivanov, H. S. Varol, D. Turchinovich, F. H. L. Koppens, M. Bonn, K. J. Tielrooij, *Nano Lett.* **2014**, *14*, 5839.
[63] G. Su, F. Wang, L. Jiang, X. Zhang, X. Su, L. Qu, Y. Lu, *J. Appl. Phys.* **2017**, *121*, 173105.
[64] Z. Xie, F. Zhang, Z. Liang, T. Fan, Z. Li, X. Jiang, H. Chen, J. Li, H. Zhang, *Photonics Res.* **2019**, *7*, 494.
[65] X. Tian, R. Wei, M. Liu, C. Zhu, Z. Luo, F. Wang, J. Qiu, *Nanoscale* **2018**, *10*, 9608.
[66] C. Pan, L. Jiang, J. Sun, Q. Wang, F. Wang, K. Wang, Y. Lu, Y. Wang, L. Qu, T. Cui, *Light: Sci. Appl.* **2020**, *9*, 80.
[67] H. Shi, R. Yan, S. Bertolazzi, J. Brivio, B. Gao, A. Kis, D. Jena, H. G. Xing, L. Huang, *ACS Nano* **2013**, *7*, 1072.
[68] T. Korn, S. Heydrich, M. Hirmer, J. Schmutzler, C. Schller, *Appl. Phys. Lett.* **2011**, *99*, 102109.
[69] D. Lagarde, L. Bouet, X. Marie, C. R. Zhu, B. L. Liu, T. Amand, P. H. Tan, B. Urbaszek, *Phys. Rev. Lett.* **2014**, *112*, 047401.
[70] A. Grubišić Čabo, J. A. Miwa, S. S. Grønborg, J. M. Riley, J. C. Johannsen, C. Cacho, O. Alexander, R. T. Chapman, E. Springate, M. Grioni, J. V. Lauritsen, P. D. C. King, P. Hofmann, S. Ulstrup, *Nano Lett.* **2015**, *15*, 5883.
[71] C. Xu, G. Zhou, E. M. Alexeev, A. R. Cadore, I. Paradisanos, A. K. Ott, G. Soavi, S. Tongay, G. Cerullo, A. C. Ferrari, O. V. Prezhdo, Z. H. Loh, *ACS Nano* **2023**, *17*, 16682.
[72] A. Roberts, D. Cormode, C. Reynolds, T. Newhouse-Illige, B. J. LeRoy, A. S. Sandhu, *Appl. Phys. Lett.* **2011**, *99*, 051912.
[73] G. Ibáñez-Redín, D. Wilson, D. Gonçalves, O. N. Oliveira, *J. Colloid. Interface Sci.* **2018**, *515*, 101.
[74] P. Li, C.-A. Tao, B. Wang, J. Huang, T. Li, J. Wang, *J. Nanosci. Nanotechnol.* **2018**, *18*, 713.
[75] A. F. M. Ibrahim, Y. S. Lin, *Chem. Eng. Sci.* **2018**, *190*, 312.
[76] X. Hu, X. Meng, J. Xiong, Z. Huang, X. Yang, L. Tan, Y. Chen, *Adv. Mater. Technol.* **2017**, *2*, 1700138.
[77] K. H. Lee, B. Lee, S.-J. Hwang, J.-U. Lee, H. Cheong, O.-S. Kwon, K. Shin, N. H. Hur, *Carbon* **2014**, *69*, 327.
[78] S. Lee, S. H. Eom, J. S. Chung, S. H. Hur, *Chem. Eng. J.* **2013**, *233*, 297.
[79] C. W. Foster, M. P. Down, Y. Zhang, X. Ji, S. J. Rowley-Neale, G. C. Smith, P. J. Kelly, C. E. Banks, *Sci. Rep.* **2017**, *7*, 42233.
[80] R. Di Santo, L. Digiacomo, S. Palchetti, V. Palmieri, G. Perini, D. Pozzi, M. Papi, G. Caracciolo, *Nanoscale* **2019**, *11*, 2733.
[81] M. Koinuma, C. Ogata, Y. Kamei, K. Hatakeyama, H. Tateishi, Y. Watanabe, T. Taniguchi, K. Gezuhara, S. Hayami, A. Funatsu, M. Sakata, Y. Kuwahara, S. Kurihara, Y. Matsumoto, *J. Phys. Chem. C* **2012**, *116*, 19822.
[82] Q. Zhang, H. Zheng, Z. Geng, S. Jiang, J. Ge, K. Fan, S. Duan, Y. Chen, X. Wang, Y. Luo, *J. Am. Chem. Soc.* **2013**, *135*, 12468.
[83] S. Kaniyankandy, S. N. Achary, S. Rawalekar, H. N. Ghosh, *J. Phys. Chem. C* **2011**, *115*, 19110.
[84] Z. Wan, S. Wang, B. Haylock, J. Kaur, P. Tanner, D. Thiel, R. Sang, I. S. Cole, X. Li, M. Lobino, Q. Li, *Carbon* **2019**, *141*, 83.
[85] I. I. Bobrinetskiy, A. V. Emelianov, S. A. Smagulova, I. A. Komarov, N. Otero, P. M. Romero, *Mater. Lett.* **2017**, *187*, 20.
[86] S. Abdolhosseinzadeh, H. Asgharzadeh, H. Seop Kim, *Sci. Rep.* **2015**, *5*, 10160.
[87] H.-M. Ju, S. H. Huh, S.-H. Choi, H.-L. Lee, *Mater. Lett.* **2010**, *64*, 357.
[88] A. G. Marrani, A. Motta, R. Schrebler, R. Zanoni, E. A. Dalchiele, *Electrochim. Acta* **2019**, *304*, 231.
[89] M. K. Rabchinskii, V. V. Shnitov, A. T. Dideikin, A. E. Aleksenskii, S. P. Vul', M. V. Baidakova, I. I. Pronin, D. A. Kirilenko, P. N. Brunkov, J. Weise, S. L. Molodtsov, *J. Phys. Chem. C* **2016**, *120*, 28261.
[90] Y.-C. Li, T.-F. Yeh, H.-C. Huang, H.-Y. Chang, C.-Y. Lin, L.-C. Cheng, C.-Y. Chang, H. Teng, S.-J. Chen, *Opt. Express* **2014**, *22*, 19726.
[91] R. Y. N. Gengler, D. S. Badali, D. Zhang, K. Dimos, K. Spyrou, D. Gournis, R. J. D. Miller, *Nat. Commun.* **2013**, *4*, 2560.
[92] M. Rogala, P. J. Kowalczyk, P. Dabrowski, I. Wlasny, W. Kozlowski, A. Busiakiewicz, S. Pawlowski, G. Dobinski, M. Smolny, I. Karaduman, L. Lipinska, R. Kozinski, K. Librant, J. Jagiello, K. Grodecki, J. M. Baranowski, K. Szot, Z. Klusek, *Appl. Phys. Lett.* **2015**, *106*, 263104.
[93] H. Li, X. Song, Y. Shi, Y. Gao, D. Si, C. Hao, *Chem. Commun.* **2019**, *55*, 1837.
[94] Y.-Q. Liu, Y.-L. Zhang, Y. Liu, H.-B. Jiang, D.-D. Han, B. Han, J. Feng, H.-B. Sun, *Chem. Rec.* **2016**, *16*, 1244.
[95] R. Arul, R. N. Oosterbeek, J. Robertson, G. Xu, J. Jin, M. C. Simpson, *Carbon* **2016**, *99*, 423.
[96] V. A. Smirnov, A. A. Arbuzov, Yu. M. Shul'ga, S. A. Baskakov, V. M. Martynenko, V. E. Muradyan, E. I. Kresova, *High Energy Chem.* **2011**, *45*, 57.
[97] S. Kang, C. C. Evans, S. Shukla, O. Reshef, E. Mazur, *Opt. Laser Technol.* **2018**, *103*, 340.
[98] W. He, C. Qin, Z. Qiao, G. Zhang, L. Xiao, S. Jia, *Carbon* **2016**, *109*, 264.
[99] R. J. W. E. Lahaye, H. K. Jeong, C. Y. Park, Y. H. Lee, *Phys. Rev. B* **2009**, *79*, 125435.
[100] M. Acik, G. Lee, C. Mattevi, M. Chhowalla, K. Cho, Y. J. Chabal, *Nat. Mater.* **2010**, *9*, 840.
[101] J. Aumanen, A. Johansson, J. Koivistoinen, P. Myllyperkiö, M. Pettersson, *Nanoscale* **2015**, *7*, 2851.
[102] I. I. Bobrinetskiy, A. V. Emelianov, N. Otero, P. M. Romero, *Appl. Phys. Lett.* **2015**, *107*, 043104.
[103] M. E. Mendoza, E. H. M. Ferreira, A. Kuznetsov, C. A. Achete, J. Aumanen, P. Myllyperkiö, A. Johansson, M. Pettersson, B. S. Archanjo, *Carbon* **2019**, *143*, 720.
[104] Y.-Z. Hong, H.-C. Tsai, Y.-H. Wang, J. Aumanen, P. Myllyperkiö, A. Johansson, Y.-C. Kuo, L.-Y. Chang, C.-H. Chen, M. Pettersson, W.-Y. Woon, *Carbon* **2018**, *129*, 396.
[105] J. Koivistoinen, J. Aumanen, V.-M. Hiltunen, P. Myllyperkiö, A. Johansson, M. Pettersson, *Appl. Phys. Lett.* **2016**, *108*, 153112.
[106] A. V. Emelianov, D. Kireev, A. Offenhäusser, N. Otero, P. M. Romero, I. I. Bobrinetskiy, *ACS Photonics* **2018**, *5*, 3107.
[107] J. Aumanen, A. Johansson, O. Herranen, P. Myllyperkiö, M. Pettersson, *Phys. Chem. Chem. Phys.* **2014**, *17*, 209.
[108] A. V. Emelianov, N. P. Nekrasov, M. V. Moskotin, G. E. Fedorov, N. Otero, P. M. Romero, V. K. Nevolin, B. I. Afinogenov, A. G. Nasibulin, I. I. Bobrinetskiy, *Adv. Electron. Mater.* **2021**, *7*, 2000872.
[109] R. R. Nair, P. Blake, A. N. Grigorenko, K. S. Novoselov, T. J. Booth, T. Stauber, N. M. R. Peres, A. K. Geim, *Science* **2008**, *320*, 1308.
[110] N. Mitoma, R. Nouchi, K. Tanigaki, *J. Phys. Chem. C* **2013**, *117*, 1453.
[111] C. L. Thomsen, D. Madsen, S. R. Keiding, J. Tho/gersen, O. Christiansen, *J. Chem. Phys.* **1999**, *110*, 3453.
[112] J. Koivistoinen, L. Sládková, J. Aumanen, P. Koskinen, K. Roberts, A. Johansson, P. Myllyperkiö, M. Pettersson, *J. Phys. Chem. C* **2016**, *120*, 22330.
[113] D. W. Boukhvalov, M. I. Katsnelson, *J. Am. Chem. Soc.* **2008**, *130*, 10697.
[114] O. Ö. Ekiz, M. Ürel, H. Güner, A. K. Mizrak, A. Dâna, *ACS Nano* **2011**, *5*, 2475.

[115] A. Johansson, H.-C. Tsai, J. Aumanen, J. Koivistoinen, P. Myllyperkiö, Y.-Z. Hung, M.-C. Chuang, C.-H. Chen, W. Y. Woon, M. Pettersson, *Carbon* **2017**, *115*, 77.
[116] I. Bobrinetskiy, A. Emelianov, A. Nasibulin, I. Komarov, N. Otero, P. M. Romero, *J. Phys. D: Appl. Phys.* **2016**, *49*, 41LT01.
[117] A. Maurice, L. Bodelot, B. K. Tay, B. Lebental, *Small* **2018**, *14*, 1801348.
[118] X. Xu, B. Shi, X. Zhang, Y. Liu, W. Cai, M. Ren, X. Jiang, R. A. Rupp, Q. Wu, J. Xu, *Opt. Express* **2018**, *26*, 20726.
[119] S. M. Lee, Y. H. Lee, Y. G. Hwang, J. R. Hahn, H. Kang, *Phys. Rev. Lett.* **1999**, *82*, 217.
[120] R. K. Raman, Y. Murooka, C.-Y. Ruan, T. Yang, S. Berber, D. Tománek, *Phys. Rev. Lett.* **2008**, *101*, 077401.
[121] J. Kanasaki, E. Inami, K. Tanimura, H. Ohnishi, K. Nasu, *Phys. Rev. Lett.* **2009**, *102*, 087402.
[122] D. Zhu, M. Qiao, J. Yan, J. Xie, H. Guo, S. Deng, G. He, Y. Zhao, M. Luo, *Nanoscale* **2023**, *15*, 14837.
[123] W. Zhang, L. Li, Z. B. Wang, A. A. Pena, D. J. Whitehead, M. L. Zhong, Z. Lin, H. W. Zhu, *Appl. Phys. A* **2012**, *109*, 291.
[124] T. Dong, M. Sparkes, C. Durkan, W. O'Neill, *J. Laser Appl.* **2016**, *28*, 022202.
[125] F. Herziger, R. Mirzayev, E. Poliani, J. Maultzsch, *Phys. Status Solidi B* **2015**, *252*, 2451.
[126] E. Kim, C. Ko, K. Kim, Y. Chen, J. Suh, S.-G. Ryu, K. Wu, X. Meng, A. Suslu, S. Tongay, J. Wu, C. P. Grigoropoulos, *Adv. Mater.* **2016**, *28*, 341.
[127] T. Afaneh, P. K. Sahoo, I. A. P. Nobrega, Y. Xin, H. R. Gutiérrez, *Adv. Funct. Mater.* **2018**, *28*, 1802949.
[128] H. I. Wang, M.-L. Braatz, N. Richter, K.-J. Tielrooij, Z. Mics, H. Lu, N.-E. Weber, K. Müllen, D. Turchinovich, M. Kläui, M. Bonn, *J. Phys. Chem. C* **2017**, *121*, 4083.
[129] S. M. Hornett, M. Heath, D. W. Horsell, E. Hendry, *Phys. Rev. B* **2014**, *90*, 081401.
[130] P. Giannozzi, R. Car, G. Scoles, *J. Chem. Phys.* **2003**, *118*, 1003.
[131] Y. Sato, K. Takai, T. Enoki, *Nano Lett.* **2011**, *11*, 3468.
[132] M. Breusing, C. Ropers, T. Elsaesser, *Phys. Rev. Lett.* **2009**, *102*, 086809.
[133] J. Hu, G. M. Vanacore, A. Cepellotti, N. Marzari, A. H. Zewail, *Proc. Natl. Acad. Sci.* **2016**, *113*, E6555.
[134] F. Carbone, P. Baum, P. Rudolf, A. H. Zewail, *Phys. Rev. Lett.* **2008**, *100*, 035501.
[135] C. Si, Z. Sun, F. Liu, *Nanoscale* **2016**, *8*, 3207.
[136] P. Koskinen, K. Karppinen, P. Myllyperkiö, V.-M. Hiltunen, A. Johansson, M. Pettersson, *J. Phys. Chem. Lett.* **2018**, *9*, 6179.
[137] A. Johansson, P. Myllyperkiö, P. Koskinen, J. Aumanen, J. Koivistoinen, H.-C. Tsai, C.-H. Chen, L.-Y. Chang, V.-M. Hiltunen, J. J. Manninen, W. Y. Woon, M. Pettersson, *Nano Lett.* **2017**, *17*, 6469.
[138] V.-M. Hiltunen, P. Koskinen, K. K. Mentel, J. Manninen, P. Myllyperkiö, A. Johansson, M. Pettersson, *J. Phys. Chem. C* **2020**, *124*, 8371.
[139] K. K. Mentel, J. Manninen, V. M. Hiltunen, P. Myllyperkiö, A. Johansson, M. Pettersson, *Nanoscale Adv.* **2021**, *3*, 1431.
[140] V. M. Hiltunen, P. Koskinen, K. K. Mentel, J. Manninen, P. Myllyperkiö, M. Pettersson, A. Johansson, *npj 2D Mater. Appl.* **2021**, *5*, 49.
[141] J. Ma, D. Alfè, A. Michaelides, E. Wang, *Phys. Rev. B* **2009**, *80*, 033407.
[142] K. Flouris, M. Mendoza Jimenez, J.-D. Debus, H. J. Herrmann, *Phys. Rev. B* **2018**, *98*, 155419.
[143] M. Tripathi, A. King, G. Fratta, M. Meloni, M. Large, J. P. Salvage, N. M. Pugno, A. B. Dalton, *ACS Omega* **2018**, *3*, 17000.
[144] A. De Sanctis, I. Amit, S. P. Hepplestone, M. F. Craciun, S. Russo, *Nat. Commun.* **2018**, *9*, 1652.
[145] V. K. Nagareddy, T. J. Octon, N. J. Townsend, S. Russo, M. F. Craciun, C. D. Wright, *Adv. Funct. Mater.* **2018**, *28*, 1804434.
[146] G. H. Han, S. J. Chae, E. S. Kim, F. Güneş, I. H. Lee, S. W. Lee, S. Y. Lee, S. C. Lim, H. K. Jeong, M. S. Jeong, Y. H. Lee, *ACS Nano* **2011**, *5*, 263.
[147] L. Hu, X. Shan, Y. Wu, J. Zhao, X. Lu, *Sci. Rep.* **2017**, *7*, 15538.
[148] D. W. Li, Y. S. Zhou, X. Huang, L. Jiang, J.-F. Silvain, Y. F. Lu, *Nanoscale* **2015**, *7*, 3651.
[149] Y. Miyamoto, H. Zhang, D. Tománek, *Phys. Rev. Lett.* **2010**, *104*, 208302.
[150] Z. Lin, X. Ye, J. Han, Q. Chen, P. Fan, H. Zhang, D. Xie, H. Zhu, M. Zhong, *Sci. Rep.* **2015**, *5*, 11662.
[151] Y. Li, L. Zhang, T. Wang, J. Xie, M. Wang, Z. Qi, Q. Cui, J. Chang, *Appl. Phys. Lett.* **2023**, *122*, 57.
[152] R. Wang, Y. Yu, S. Zhou, H. Li, H. Wong, Z. Luo, L. Gan, T. Zhai, R. Y. Wang, Y. W. Yu, S. S. Zhou, H. Q. Li, L. Gan, T. Y. Zhai, H. L. Wong, Z. T. Luo, *Adv. Funct. Mater.* **2018**, *28*, 1802473.
[153] W. Li, X. Qian, J. Li, *Nat. Rev. Mater.* **2021**, *6*, 829.
[154] X. Qian, J. Liu, L. Fu, J. Li, *Science* **2014**, *346*, 1344.
[155] F. Xia, H. Wang, D. Xiao, M. Dubey, A. Ramasubramaniam, *Nat. Photonics* **2014**, *8*, 899.
[156] F. Zheng, C. Cai, S. Ge, X. Zhang, X. Liu, H. Lu, Y. Zhang, J. Qiu, T. Taniguchi, K. Watanabe, S. Jia, J. Qi, J.-H. Chen, D. Sun, J. Feng, *Adv. Mater.* **2016**, *28*, 4845.
[157] K. A. N. Duerloo, E. J. Reed, *ACS Nano* **2016**, *10*, 289.
[158] K. Sun, S. Sun, C. Zhu, H. Tian, H. Yang, J. Li, *Sci. Adv.* **2018**, *4*, eaas9660.
[159] F. Lavini, M. Rejhon, E. Riedo, *Nat. Rev. Mater.* **2022**, *7*, 814.
[160] T. Suzuki, R. Hida, Y. Yamaguchi, K. Nakagawa, T. Saiki, F. Kannari, *App. Phys. Express* **2017**, *10*, 092502.
[161] T. Kunkel, Y. Vorobyov, M. Smayev, P. Lazarenko, A. Romashkin, S. Kozyukhin, *Mater. Sci. Semicond. Process.* **2022**, *139*, 106350.
[162] B. Liu, S. Liu, L. Yang, Z. Chen, E. Zhang, Z. Li, J. Wu, X. Ruan, F. Xiu, W. Liu, L. He, R. Zhang, Y. Xu, *Phys. Rev. Lett.* **2020**, *125*, 267205.
[163] S. Raoux, W. Wełnic, D. Lelmini, *Chem. Rev.* **2010**, *110*, 240.
[164] Y. Deng, Y. Yu, Y. Song, J. Zhang, N. Z. Wang, Z. Sun, Y. Yi, Y. Z. Wu, S. Wu, J. Zhu, J. Wang, X. H. Chen, Y. Zhang, *Nature* **2018**, *563*, 94.
[165] X. Xu, T. Wang, P. Chen, C. Zhou, J. Ma, D. Wei, H. Wang, B. Niu, X. Fang, D. Wu, S. Zhu, M. Gu, M. Xiao, Y. Zhang, *Nature* **2022**, *609*, 496.
[166] G. Lu, K. Yu, Z. Wen, J. Chen, *Nanoscale* **2013**, *5*, 1353.
[167] Y. W. Son, M. L. Cohen, S. G. Louie, *Phys. Rev. Lett.* **2006**, *97*, 216803.
[168] M. Y. Han, B. Özyilmaz, Y. Zhang, P. Kim, *Phys. Rev. Lett.* **2007**, *98*, 206805.
[169] X. Yang, X. Dou, A. Rouhanipour, L. Zhi, H. J. Räder, K. Müllen, *J. Am. Chem. Soc.* **2008**, *130*, 4216.
[170] T. Yang, H. Lin, X. Zheng, K. P. Loh, B. Jia, *J. Mater. Chem. A: Mater.* **2017**, *5*, 16537.
[171] L. Guo, Y.-L. Zhang, D.-D. Han, H.-B. Jiang, D. Wang, X.-B. Li, H. Xia, J. Feng, Q.-D. Chen, H.-B. Sun, *Adv. Opt. Mater.* **2014**, *2*, 120.
[172] R. Bueno, M. Marciello, M. Moreno, C. Sánchez-Sánchez, J. I. Martinez, L. Martinez, E. Prats-Alfonso, A. Guimerà-Brunet, J. A. Garrido, R. Villa, F. Mompean, M. García-Hernandez, Y. Huttel, M. d. P. Morales, C. Briones, M. F. López, G. J. Ellis, L. Vázquez, J. A. Martín-Gago, *ACS Omega* **2019**, *4*, 3287.
[173] N. Peimyoo, J. Li, J. Shang, X. Shen, C. Qiu, L. Xie, W. Huang, T. Yu, *ACS Nano* **2012**, *6*, 8878.
[174] H. Lee, K. Paeng, I. S. Kim, *Sznth. Met.* **2018**, *244*, 36.
[175] C. J. Docherty, C.-T. Lin, H. J. Joyce, R. J. Nicholas, L. M. Herz, L.-J. Li, M. B. Johnston, *Nat. Commun.* **2012**, *3*, 1228.
[176] D. Usachov, O. Vilkov, A. Grüneis, D. Haberer, A. Fedorov, V. K. Adamchuk, A. B. Preobrajenski, P. Dudin, A. Barinov, M. Oehzelt, C. Laubschat, D. V. Vyalikh, *Nano Lett.* **2011**, *11*, 5401.
[177] A. Lampinen, E. See, A. Emelianov, P. Myllyperkiö, A. Johansson, M. Pettersson, *Phys. Chem. Chem. Phys.* **2023**, *25*, 10778.

[178] K. H. Ibrahim, M. Irannejad, B. Wales, J. Sanderson, M. Yavuz, K. P. Musselman, *Adv. Opt. Mater.* **2018**, *6*, 1701365.
[179] P. Zuo, L. Jiang, X. Li, P. Ran, B. Li, A. Song, M. Tian, T. Ma, B. Guo, L. Qu, Y. Lu, *Nanoscale* **2019**, *11*, 485.
[180] J. Huo, G. Zou, Y. Xiao, T. Sun, B. Feng, D. Shen, C. Du, J. Peng, L. Lin, L. Liu, *Nano Energy* **2023**, *113*, 108548.
[181] A. Shahin, K. Ibrahim, F. Ye, R. Karimi, J. Sanderson, K. P. Musselman, *Sens. Actuators, B* **2022**, *359*, 131576.
[182] B. Li, L. Jiang, X. Li, P. Ran, P. Zuo, A. Wang, L. Qu, Y. Zhao, Z. Cheng, Y. Lu, *Sci. Rep.* **2017**, *7*, 11182.
[183] I. Paradisanos, E. Kymakis, C. Fotakis, G. Kioseoglou, E. Stratakis, *Appl. Phys. Lett.* **2014**, *105*, 041108.
[184] P. Zuo, L. Jiang, X. Li, M. Tian, L. Ma, C. Xu, Y. Yuan, X. Li, X. Chen, M. Liang, *J. Phys. Chem. C* **2021**, *125*, 8304.
[185] P. Russo, A. Hu, G. Compagnini, W. W. Duley, N. Y. Zhou, *Nanoscale* **2014**, *6*, 2381.
[186] X. Li, X. Li, L. Jiang, P. Zuo, Y. Zhao, S. Wang, X. Chen, M. Liang, L. Ma, *Carbon* **2021**, *185*, 384.
[187] P. Zuo, L. Jiang, X. Li, M. Tian, C. Xu, Y. Yuan, P. Ran, B. Li, Y. Lu, *ACS Appl. Mater. Interfaces* **2019**, *11*, 39334.
[188] W. Zhang, Q. Wang, Y. Chen, Z. Wang, A. T. S. Wee, *2D Mater.* **2016**, *3*, 022001.
[189] A. K. Geim, I. V. Grigorieva, *Nature* **2013**, *499*, 419.
[190] Y. Liu, Z. Gao, Y. Tan, F. Chen, *ACS Nano* **2018**, *12*, 10529.
[191] M. Fortin-Deschênes, K. Watanabe, T. Taniguchi, F. Xia, *Nat. Mater.* **2024**, *23*, 339.
[192] C. Trovatello, G. Piccinini, S. Forti, F. Fabbri, A. Rossi, S. De Silvestri, C. Coletti, G. Cerullo, S. Dal Conte, *npj 2D Mater. Appl.* **2022**, *6*, 1.
[193] A. Bian, S. Fu, P. Wang, K. Zhao, J. He, X. Zhang, D. He, Y. Wang, H. Zhao, *J. Mater. Chem. C: Mater.* **2022**, *10*, 5328.
[194] Z. Hu, X. Liu, P. L. Hernández-Martínez, S. Zhang, P. Gu, W. Du, W. Xu, H. V. Demir, H. Liu, Q. Xiong, *InfoMat* **2022**, *4*, e12290.
[195] C. Wang, L. Cusin, C. Ma, E. Unsal, H. Wang, V. Girelli Consolaro, V. Montes-García, B. Han, S. Vitale, A. Dianat, A. Croy, H. Zhang, R. Gutierrez, G. Cuniberti, Z. Liu, L. Chi, A. Ciesielski, P. Samorì, *Adv. Mater.* **2023**, *36*, 2305882.
[196] Y. Garcia-Basabe, A. R. Rocha, F. C. Vicentin, C. E. P. Villegas, R. Nascimento, E. C. Romani, E. C. de Oliveira, G. J. M. Fechine, S. Li, G. Eda, D. G. Larrude, *Phys. Chem. Chem. Phys.* **2017**, *19*, 29954.
[197] J. Peng, G. Zou, J. Huo, Y. Xiao, T. Sun, Z. Li, B. Feng, L. Liu, *Nano Energy* **2023**, *117*, 108891.
[198] T. Zou, B. Zhao, W. Xin, Y. Wang, B. Wang, X. Zheng, H. Xie, Z. Zhang, J. Yang, C. Guo, *Light: Sci. Appl.* **2020**, *9*, 69.
[199] T. Zou, B. Zhao, W. Xin, F. Wang, H. Xie, Y. Li, Y. Shan, K. Li, Y. Sun, J. Yang, *Nano Res.* **2022**, *15*, 4490.
[200] B. W. Su, B. W. Yao, X. L. Zhang, K. X. Huang, D. K. Li, H. W. Guo, X. K. Li, X. D. Chen, Z. B. Liu, J. G. Tian, *Nanoscale Adv.* **2020**, *2*, 1733.
[201] J. An, T.-S. D. Le, C. Huat, J. Lim, V. T. Tran, Z. Zhan, Y. Gao, L. Zheng, G. Sun, Y.-J. Kim, *Adv. Sci.* **2018**, *5*, 1800496.
[202] K. Mistry, K. H. Ibrahim, I. Novodchuk, H. T. Ngo, G. Imamura, J. Sanderson, M. Yavuz, G. Yoshikawa, K. P. Musselman, *Adv. Mater. Technol.* **2020**, *5*, 2000704.
[203] Y. Guan, Y. Ding, Y. Fang, G. Wang, S. Zhao, L. Wang, J. Huang, M. Chen, J. Hao, C. Xu, L. Zhen, F. Huang, Y. Li, L. Yang, *Small* **2023**, *19*, 2303654.
[204] C. Qin, Z. Qiao, W. He, Y. Gong, G. Zhang, R. Chen, Y. Gao, L. Xiao, S. Jia, *J. Mater. Chem. C* **2018**, *6*, 2329.
[205] M. T. Turunen, E. Hulkko, K. K. Mentel, X. Bai, S.-T. Akkanen, M. Amini, S. Li, H. Lipsanen, M. Pettersson, Z. Sun, *Adv. Mater. Interfaces* **2021**, *8*, 2002119.
[206] X. Li, Q. Zhang, X. Chen, M. Gu, *Sci. Rep.* **2013**, *3*, 2819.
[207] X. Li, H. Ren, X. Chen, J. Liu, Q. Li, C. Li, G. Xue, J. Jia, L. Cao, A. Sahu, B. Hu, Y. Wang, G. Jin, M. Gu, *Nat. Commun.* **2015**, *6*, 6984.
[208] M. Kasischke, S. Maragkaki, S. Volz, A. Ostendorf, E. L. Gurevich, *Appl. Surf. Sci.* **2018**, *445*, 197.
[209] M. Gu, Q. Zhang, S. Lamon, *Nat. Rev. Mater.* **2016**, *1*, 16070.
[210] Z. Qiao, C. Qin, W. He, Y. Gong, B. Li, G. Zhang, R. Chen, Y. Gao, L. Xiao, S. Jia, *Carbon* **2019**, *142*, 224.
[211] X. Gao, S. Pandey, M. Kianinia, J. Ahn, P. Ju, I. Aharonovich, N. Shivaram, T. Li, *ACS Photonics* **2021**, *8*, 994.
[212] Y. Z. Yang, T. X. Zhu, Z. P. Li, X. D. Zeng, N. J. Guo, S. Yu, Y. Meng, Z. A. Wang, L. K. Xie, Z. Q. Zhou, Q. Li, J. S. Xu, X. Y. Gao, W. Liu, Y. T. Wang, J. S. Tang, C. F. Li, G. C. Guo, *ACS Appl. Nano Mater.* **2023**, *6*, 6407.
[213] S. Hou, M. D. Birowosuto, S. Umar, M. A. Anicet, R. Y. Tay, P. Coquet, B. K. Tay, H. Wang, E. H. T. Teo, *2D Mater.* **2017**, *5*, 015010.
[214] J. Yan, S. Deng, D. Zhu, H. Bai, H. Zhu, *Nano Energy* **2022**, *97*, 107188.
[215] J. Huo, G. Zou, Y. Xiao, T. Sun, B. Feng, D. Shen, L. Lin, W. Wang, A. Zhanwen, L. Liu, *Mater. Horiz.* **2023**, *10*, 524.
[216] Y. Zhang, X. Wang, K. Yan, H. Zhu, B. Wang, B. Zou, *Adv. Funct. Mater.* **2023**, *33*, 2211272.
[217] X. Ye, M. Qi, Y. Yang, M. Yu, T. Huang, J. Zhang, X. Yuan, G. Suo, X. Hou, L. Feng, L. Zhang, Y. Yang, *Adv. Mater. Technol.* **2020**, *5*, 2000446.
[218] Z. Gan, Y. Cao, R. A. Evans, M. Gu, *Nat. Commun.* **2013**, *4*, 2061.
[219] V. Harinarayana, Y. C. Shin, *Opt. Laser Technol.* **2021**, *142*, 107180.
[220] Z. Lin, M. Hong, *Ultrafast Science* **2021**, 9783514.
[221] Y. Li, M. Hong, *Laser Photon. Rev.* **2020**, *14*, 1900062.
[222] J. Schirmer, E. Iatta, A. V. Emelianov, M. Nissinen, M. Pettersson, *Adv. Mater. Interfaces* **2024**, *11*, 2300870.
[223] N. Nekrasov, N. Yakunina, V. Nevolin, I. Bobrinetskiy, P. Vasilevsky, A. Y. Gerasimenko, *Biomimetics* **2021**, *6*, 66.
[224] H. Hamidi, J. Levieux, C. Larrigy, A. Russo, E. Vaughan, R. Murray, A. J. Quinn, D. Iacopino, *Biosens. Bioelectron. X* **2023**, *15*, 100403.
[225] S. K. Thomas, W. D. Jamieson, R. E. A. Gwyther, B. J. Bowen, A. Beachey, H. L. Worthy, J. E. Macdonald, M. Elliott, O. K. Castell, D. D. Jones, *Bioconjug. Chem.* **2020**, *31*, 584.
[226] A. J. Zaki, A. M. Hartley, S. C. Reddington, S. K. Thomas, P. Watson, A. Hayes, A. V. Moskalenko, M. F. Craciun, J. E. Macdonald, D. D. Jones, M. Elliott, *RSC Adv.* **2018**, *8*, 5768.
[227] R. E. A. Gwyther, N. P. Nekrasov, A. V Emelianov, A. G. Nasibulin, K. Ramakrishnan, I. Bobrinetskiy, D. D. Jones, *Adv. Funct. Mater.* **2022**, *32*, 2112374.
[228] E. D. Sitsanidis, J. Schirmer, A. Lampinen, K. K. Mentel, V. M. Hiltunen, V. Ruokolainen, A. Johansson, P. Myllyperkiö, M. Nissinen, M. Pettersson, *Nanoscale Adv.* **2021**, *3*, 2065.
[229] A. A. Tregubov, P. I. Nikitin, M. P. Nikitin, *Chem. Rev.* **2018**, *118*, 10294.
[230] M. E. Schmidt, M. Muruganathan, T. Kanzaki, T. Iwasaki, A. M. M Hammam, S. Suzuki, S. Ogawa, H. Mizuta, *Small* **2019**, *15*, 1903025.
[231] J. Zhao, P. Ji, Y. Li, R. Li, K. Zhang, H. Tian, K. Yu, B. Bian, L. Hao, X. Xiao, W. Griffin, N. Dudeck, R. Moro, L. Ma, W. A. de Heer, *Nature* **2024**, *625*, 60.
[232] K. K. Mentel, A. V Emelianov, A. Philip, A. Johansson, M. Karppinen, M. Pettersson, *Adv. Mater. Interfaces* **2022**, *9*, 2201110.
[233] T. Knobloch, B. Uzlu, Y. Y. Illarionov, Z. Wang, M. Otto, L. Filipovic, M. Waltl, D. Neumaier, M. C. Lemme, T. Grasser, *Nat. Electron.* **2022**, *5*, 356.
[234] Z. Zhang, Z. Tian, Y. Mei, Z. Di, *Mater. Sci. Eng., R Rep.* **2021**, *145*, 100621.
[235] C. Dai, Y. Rho, K. Pham, B. McCormick, B. W. Blankenship, W. Zhao, Z. Zhang, S. M. Gilbert, M. F. Crommie, F. Wang, C. P. Grigoropoulos, A. Zettl, *Nano Lett.* **2022**, *22*, 5301.

[236] J. Mao, S. P. Milovanović, M. Anđelković, X. Lai, Y. Cao, K. Watanabe, T. Taniguchi, L. Covaci, F. M. Peeters, A. K. Geim, Y. Jiang, E. Y. Andrei, *Nature* **2020**, *584*, 215.
[237] K. A. Drogowska-Horna, I. Mirza, A. Rodriguez, P. Kovaříček, J. Sládek, T. J. Y. Derrien, M. Gedvilas, G. Račiukaitis, O. Frank, N. M. Bulgakova, M. Kalbáč, *Nano Res.* **2020**, *13*, 2332.
[238] H. W. Guo, Z. Hu, Z. B. Liu, J. G. Tian, *Adv. Funct. Mater.* **2021**, *31*, 2007810.
[239] X. Zhang, Y. Zhang, H. Yu, H. Zhao, Z. Cao, Z. Zhang, Y. Zhang, *Adv. Mater.* **2023**, *35*, 2207966.
[240] Y. Meng, J. Feng, S. Han, Z. Xu, W. Mao, T. Zhang, J. S. Kim, I. Roh, Y. Zhao, D. H. Kim, Y. Yang, J. W. Lee, L. Yang, C. W. Qiu, S. H. Bae, *Nat. Rev. Mater.* **2023**, *8*, 498.
[241] C. Jiang, X. Wang, H. Wang, S. Wang, L. Qin, J. Liu, Z. Zhang, *Adv. Photonics Res.* **2022**, *3*, 2100183.
[242] M. S. Choi, A. Nipane, B. S. Y. Kim, M. E. Ziffer, I. Datta, A. Borah, Y. Jung, B. Kim, D. Rhodes, A. Jindal, Z. A. Lamport, M. Lee, A. Zangiabadi, M. N. Nair, T. Taniguchi, K. Watanabe, I. Kymissis, A. N. Pasupathy, M. Lipson, X. Zhu, W. J. Yoo, J. Hone, J. T. Teherani, *Nat. Electron.* **2021**, *4*, 731.